

1 **Shakedown analysis of engineering structures under multiple variable**
2 **mechanical and thermal loads using the stress compensation method**

3 Heng Peng^a, Yinghua Liu^{a,*}, Haofeng Chen^b and Jun Shen^a

4 ^a*Department of Engineering Mechanics, AML, Tsinghua University, Beijing 100084, People's Republic of China*

5 ^b*Department of Mechanical and Aerospace Engineering, University of Strathclyde, Glasgow G1 1XJ, UK*

6 *Corresponding author: yhliu@mail.tsinghua.edu.cn

7
8 **Abstract**

9 The determination of shakedown load or shakedown domain is an important task in
10 structural design and integrity assessment. In this paper, a novel numerical procedure based
11 on the Stress Compensation Method (SCM) is developed to perform shakedown analysis of
12 engineering structures under multiple variable mechanical and thermal loads. By applying the
13 compensation stress on the yield regions that occur at every load vertex of the prescribed
14 loading domain to adjust the total stress to the yield surface and re-solving the equilibrium
15 equations, the statically admissible residual stress field for static shakedown analysis is
16 constructed. A robust and effective iteration control technique with some convergence
17 parameters is used to check the change of the compensation stress in the inner loop and to
18 update the shakedown load multiplier in the outer loop. For the purpose of general use, the
19 method is implemented into ABAQUS platform. The shakedown problems for the Bree plate,
20 a square plate with a central circular hole and a practical thick vessel with nozzles under some
21 two-dimensional and three-dimensional loading domains are effectively solved and analyzed.
22 Both alternating plasticity mechanism and ratcheting mechanism to determine the shakedown
23 boundary of these structures are revealed. Numerical applications show that the proposed
24 method has good numerical stability, high accuracy and efficiency, and is well suited for
25 shakedown analysis of large-scale practical engineering structures.

26 *Keywords:* Plasticity; Shakedown analysis; Stress Compensation Method; Cyclic loading;
27 Multi-dimensional loading domain

29 **1 Introduction**

30 In many practical engineering fields, such as electric power, nuclear energy, aerospace,
31 petrochemical and civil industries, structural components are usually subjected to variable
32 repeated mechanical and thermal loads. On the one hand, for making full use of the
33 load-carrying capability of materials, these structural components are allowed to operate in
34 plasticity state. On the other hand, in order to ensure structures to be safe and serviceable, the
35 applied variable loads cannot be beyond the safety margin, i.e. shakedown domain, so that the
36 structural components cannot fail due to alternating plasticity (low-cycle fatigue) or ratcheting
37 (incremental collapse). Therefore, the shakedown analysis has a wide application prospect
38 because of its important theoretical significance and practical engineering value for
39 strengthening the security of structures and reducing costs. Moreover, the determination of
40 shakedown load or shakedown domain of structures becomes the important task in structural
41 design and integrity assessment.

42 Many designers hope to determine the shakedown limit by the step-by-step incremental
43 elastic-plastic analysis [1, 2], but for complicated loading history the computation is
44 cumbersome and time-consuming. In addition, the exact loading history is often uncertain in
45 practical situations. The shakedown analysis [3-6] based on the lower bound theorem by
46 Melan [3] and the upper bound theorem by Koiter [4] provides an effective approach to
47 calculating the shakedown limit of structures, where the exact loading history is not
48 concerned but only the bounding box of these loads. Since the two classical shakedown
49 theorems [3, 4] were established, the studies on shakedown analysis have attracted broad
50 attention in structural engineering and academic circles (see Refs. [5-44]), mainly involving
51 the theoretical extensions [5-16] and development of numerical methods [7, 17-44] for
52 shakedown analysis.

53 The two classical shakedown theorems rest on the assumptions [5] of perfectly plastic
54 material, associated temperature-independent constitutive laws, small displacement,
55 negligible inertia and creeping effects. In some engineering situations, these assumptions may
56 be unrealistic. To extend the theory to make it applied in more practical applications, some
57 researchers [6-16] got rid of some coercive assumptions. The shakedown problems of

58 non-associated flow rules [6, 7], geometrical nonlinearities [8], dynamic effects [9, 10],
59 damaging inelastic material [11, 13] and nonlinear kinematic hardening material [12-16] have
60 been investigated.

61 However, although the shakedown theories are proposed and extended, a bigger difficulty
62 in practical engineering applications lies on the numerical method for solving the shakedown
63 problem. Shakedown analysis based on the upper and lower bound theorem is mostly
64 transformed as a mathematical programming problem [7, 17-29], which aims to minimize or
65 maximize a goal function with plenty of independent variables and constraint conditions [17].
66 As one of pioneers in limit and shakedown analysis field, Maier [6] adapted shakedown
67 theory to the linear programming method using piecewise linearization of yield surfaces. If
68 the von Mises yield criterion is used, the mathematical programming formulation for
69 shakedown analysis leads to a complicated nonlinear optimization problem. Over the last four
70 decades, with the rapid development of numerical methods, some powerful algorithms such
71 as the nonlinear Newton-type iteration algorithm [7, 20-22], the second order cone
72 programming (SQCP) [23, 24] and the interior point method (IPM) [25-29] have been
73 developed to solve the nonlinear optimization problem. Besides, some other computational
74 methods [30-35] of structural analysis instead of traditional finite element method have been
75 combined with shakedown theory to solve the shakedown problem.

76 Going around the difficulties of optimization, Ponter and Chen [36-39, 45] developed the
77 elastic compensation method (ECM) or the linear matching method (LMM) to solve the
78 shakedown problem. Using more physical arguments, the LMM matches the linear behavior
79 to the nonlinear plastic behavior by performing a sequence of linear solutions with spatially
80 varying moduli [38], and the incompressible and kinematically admissible strain rate history
81 is also constructed at the same time. Then a series of monotonically reducing upper bounds
82 are generated by an iterative scheme making full use of the upper shakedown theorem. More
83 recently, the residual stress decomposition method for shakedown (RSDM-S) [41, 46] was
84 proposed for the shakedown analysis of some simple two-dimensional structures under
85 mechanical and thermal loads.

86 Using these proposed numerical methods, the shakedown limits or shakedown domains of
87 some structures such as tubes, holed plates, continuous beams, pressure vessels and piping,

88 are calculated. However, it should be mentioned that most of these applications are restricted
89 to some specific cases (plane problem and axisymmetric shells under two loads) and the
90 computational models are relatively simple. In practical industrial applications, engineering
91 structures are often complex and subjected to multiple variable loads. After mesh
92 discretization, the large number of optimization variables and constraints generally result in a
93 tremendous mathematical programming problem, which implies these methods are of low
94 computational efficiency. Moreover, the computing scale of the mathematical programming
95 problem is multiplied with the increase of the vertices of the loading domain.

96 The purpose of this paper is to develop a novel and effective numerical procedure based
97 on the Stress Compensation Method (SCM) to solve the practical shakedown problems of
98 large-scale engineering structures under multiple variable mechanical and thermal loads.
99 Differing from the LMM that modifies elastic moduli of the material to match the stress to the
100 yield surface, the SCM directly adjusts the stress to the yield surface by applying the
101 compensation stress on the yield regions. The residual stresses for static shakedown analysis
102 are calculated iteratively at the end of a load cycle instead of at every load vertex, by which
103 the proposed method achieves the good performance that the computational time has little
104 relationship with the number of dimensions of loading domain. Moreover, an iterative
105 procedure rather than mathematical programming formulation is established to generate a
106 sequence of descending load multipliers approaching to the shakedown limit. Over the whole
107 procedure, the global stiffness matrix is decomposed only once, which ensures the high
108 computational efficiency of shakedown analysis regardless of the number of the vertices of
109 the loading domain. Different types of Bree problem with two-dimensional loading domain
110 are tested for the verification purpose of the proposed method. A square plate with a central
111 circular hole considering different load combinations in three-dimensional loading space is
112 calculated and analyzed. Finally, the method is effectively applied for solving the practical
113 shakedown problems of a thick vessel with nozzles from nuclear reactor plant.

114 **2 Basic theory of shakedown analysis**

115 If a structure made up of elastic-perfectly plastic material is subjected to some complex

116 cyclic history of mechanical and thermal loads, the following situations are possible with the
117 increase of the applied loads [5]:

118 (1) Elastic behavior: If the loads remain sufficiently low, the structural response is perfectly
119 elastic throughout the cycle.

120 (2) Shakedown: The plastic deformation occurs in some local parts of the structure during the
121 initial several load cycles. Afterwards, the development of plastic deformation terminates
122 and the body possesses a time-independent residual stress field that keeps the total stress
123 within yield.

124 (3) Alternating plasticity: The plastic strain increments change sign in every load cycle, but
125 the accumulation of strains over the cycle is equal to zero.

126 (4) Ratcheting: The plastic strains will accumulate in every load cycle. Moreover, the total
127 strains can become so large after a number of cycles that the structure departs from its
128 original form and loses its serviceability.

129 (5) Plastic collapse: If the loads become sufficiently high, the body plastically collapses at the
130 first load cycle.

131 The main purpose of the shakedown analysis is to evaluate the shakedown limits or
132 loading domains of structures under variable repeated loads.

133 **2.1 Static shakedown theorem by Melan**

134 As formulated for a three-dimensional situation by Melan [3] in 1938, the static
135 shakedown theorem can be stated as follows: the structure will shake down to the variable
136 repeated loads, i.e., its behavior after several initial load cycles will become purely elastic, if
137 there exists a time-independent distribution of residual stress field $\boldsymbol{\rho}(\mathbf{x})$ such that its
138 superposition with the fictitious elastic stress field $\boldsymbol{\sigma}^E(\mathbf{x}, t)$ multiplying by a multiplier λ ,
139 satisfies yield criterion of material at any point of the structure under any combination of
140 loads inside prescribed limit, namely:

$$141 \quad \boldsymbol{\sigma}(\mathbf{x}, t) = \lambda \boldsymbol{\sigma}^E(\mathbf{x}, t) + \boldsymbol{\rho}(\mathbf{x}) \quad (1)$$

$$\begin{aligned}
142 \quad & f(\boldsymbol{\sigma}(\mathbf{x}, t)) \leq 0 & \forall \mathbf{x} \in \boldsymbol{\Omega}, \forall t \\
& \nabla \cdot \boldsymbol{\rho}(\mathbf{x}) = \mathbf{0} & \text{in } \boldsymbol{\Omega} \\
& \boldsymbol{\rho}(\mathbf{x}) \cdot \mathbf{n} = \mathbf{0} & \text{on } \Gamma_f
\end{aligned} \tag{2}$$

143 Here, $\boldsymbol{\sigma}(\mathbf{x}, t)$ is the total stress field; $f(\cdot)$ denotes the yield function; λ is the shakedown
144 load multiplier; $\nabla \cdot$ denotes the divergence operator; $\boldsymbol{\rho}(\mathbf{x})$ represents a self-equilibrated
145 residual stress field which satisfies the equilibrium conditions within the body $\boldsymbol{\Omega}$ and the
146 boundary conditions on the part Γ_f of the surface; and \mathbf{n} is the unit outward normal vector
147 of the boundary Γ_f .

148 2.2 Loading domain and shakedown load multiplier

149 If a structure is subjected to an arbitrary finite number N of loadings $\mathbf{P}_i(\mathbf{x}, t)$. The
150 loading history $\mathbf{P}(\mathbf{x}, t)$ can be described as the combinations of the N loading cases, where
151 each loading case $\mathbf{P}_i(\mathbf{x}, t)$ can be decided by time-dependent multiplier $\mu_i(t)$ and the
152 constant load system $\mathbf{P}_i^0(\mathbf{x})$, that is

$$153 \quad \mathbf{P}(\mathbf{x}, t) = \sum_{i=1}^N \mathbf{P}_i(\mathbf{x}, t) = \sum_{i=1}^N \mu_i(t) \mathbf{P}_i^0(\mathbf{x}) \tag{3}$$

154 If the bounding values of each multiplier are given as follows:

$$155 \quad \mu_i^- \leq \mu_i(t) \leq \mu_i^+, \quad i = 1, \dots, N \tag{4}$$

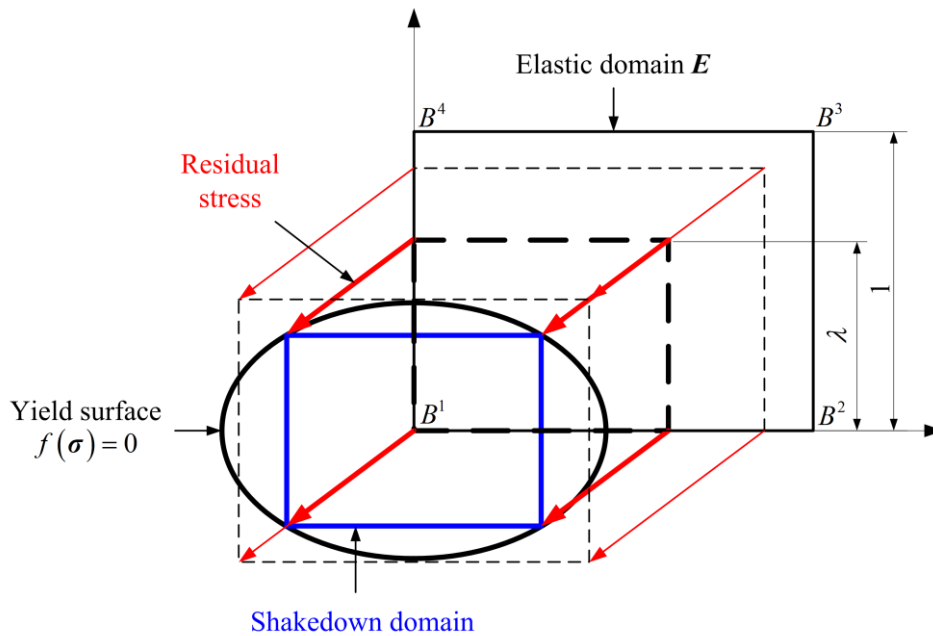
156 Eq. (3) will describe a domain $\boldsymbol{\Omega}$ of these loads. The loading domain $\boldsymbol{\Omega}$ is usually a
157 convex hyper-polyhedron defined by the vertices in the space of load parameters.

158 For an elastic body, the elastic stress field is unique to the applied loads of the structure.
159 Thus, the loading domain $\boldsymbol{\Omega}$ will produce the unique domain \mathbf{E} of the elastic stress at every
160 point of the body. As shown in Fig. 1, a two-dimensional fictitious elastic domain \mathbf{E} with four
161 vertices B^1, B^2, B^3, B^4 is taken as an example. If the applied loads (or the structural stresses)
162 vary within the loading domain $\boldsymbol{\Omega}$ (or the fictitious elastic domain \mathbf{E}), the structural safety
163 with respect to shakedown can be evaluated by a multiplier λ which is called shakedown

164 load multiplier being used for zooming the loading domain Ω and allowing for the
 165 shakedown of the structure.

166 2.3 A geometrical interpretation of static shakedown analysis

167 From the geometrical point of view, the basic ideas of static shakedown analysis can be
 168 illustrated in Fig. 1. The elastic domain E at every point of a structure should be placed into
 169 the geometric space formed by the yield surface $f(\sigma)=0$. However, all these elastic
 170 domains E can only be adjusted by means of translation and scaling, and the mutual
 171 movement among these elastic domains must satisfy certain inherent relations. The
 172 corresponding physical interpretation is as follows: the translation of these elastic domains
 173 compels the residual stress to be constant over a load cycle; the inherent relations represent
 174 the self-equilibrium conditions of the residual stress field of the whole body; and the
 175 maximum scaling factor is the shakedown load multiplier. Thus, the most critical task for
 176 shakedown analysis is to search the optimum residual stress field.



177

178 **Fig. 1.** Illustration of the basic ideas of static shakedown theorem.

179 3 Novel SCM for mechanical and thermal loads

180 We suppose that the structure is made up of elastic-perfectly plastic material obeying the

181 Drucker's postulate. The strain rate $\dot{\boldsymbol{\varepsilon}}(t)$ is decomposed into three parts:

$$182 \quad \dot{\boldsymbol{\varepsilon}}(t) = \lambda [\dot{\boldsymbol{\varepsilon}}^E(t) + \dot{\boldsymbol{\varepsilon}}_\theta(t)] + \dot{\boldsymbol{\varepsilon}}_r(t) \quad (5)$$

183 where $\dot{\boldsymbol{\varepsilon}}^E(t)$ is the elastic strain rate corresponding to the fictitious elastic stress rate $\dot{\boldsymbol{\sigma}}^E(t)$;

184 $\dot{\boldsymbol{\varepsilon}}_\theta(t)$ is the thermal strain rate; and $\dot{\boldsymbol{\varepsilon}}_r(t)$ is the residual strain rate. It is worth noting that

185 the residual strain rate $\dot{\boldsymbol{\varepsilon}}_r(t)$ consists of the plastic part $\dot{\boldsymbol{\varepsilon}}^p(t)$ and the elastic part $\dot{\boldsymbol{\varepsilon}}_r^e(t)$,

186 and the elastic term $\dot{\boldsymbol{\varepsilon}}_r^e(t)$ is generated to satisfy the deformation compatibility of the whole

187 body. Then Eq. (5) is written as

$$188 \quad \dot{\boldsymbol{\varepsilon}}(t) = \lambda [\dot{\boldsymbol{\varepsilon}}^E(t) + \dot{\boldsymbol{\varepsilon}}_\theta(t)] + \dot{\boldsymbol{\varepsilon}}^p(t) + \dot{\boldsymbol{\varepsilon}}_r^e(t) \quad (6)$$

189 According to the constitutive law of elastic-perfectly plastic material with the associated
190 flow rule, the stresses and strains are related by:

$$191 \quad \dot{\boldsymbol{\sigma}}^E(t) = \mathbf{D} \cdot \dot{\boldsymbol{\varepsilon}}^E(t) \quad (7)$$

$$192 \quad \dot{\boldsymbol{\rho}}(t) = \mathbf{D} \cdot \dot{\boldsymbol{\varepsilon}}_r^e(t) \quad (8)$$

$$193 \quad \dot{\boldsymbol{\varepsilon}}^p(t) = \gamma \frac{\partial f}{\partial \boldsymbol{\sigma}} \quad (9)$$

194 where \mathbf{D} is the elastic stiffness matrix; f is the yield function; $\dot{\boldsymbol{\varepsilon}}^p(t)$ is the plastic strain rate

195 whose direction is along the outer normal of the yield surface; and γ is the plastic

196 multiplier.

197 For a finite element model, the strains and the stresses are calculated at the Gauss points

198 of the element. The strain rate $\dot{\boldsymbol{\varepsilon}}(t)$ at the Gauss point is related to the nodal displacement

199 rate $\dot{\mathbf{u}}(t)$ of the element:

$$200 \quad \dot{\boldsymbol{\varepsilon}}(t) = \mathbf{B} \cdot \dot{\mathbf{u}}(t) \quad (10)$$

201 where \mathbf{B} is the strain-displacement matrix.

202 Substituting Eq. (6) into (8), the residual stress rate at the Gauss point is written as

$$203 \quad \dot{\boldsymbol{\rho}}(t) = \mathbf{D} \cdot \left\{ \dot{\boldsymbol{\varepsilon}}(t) - \lambda [\dot{\boldsymbol{\varepsilon}}^E(t) + \dot{\boldsymbol{\varepsilon}}_\theta(t)] - \dot{\boldsymbol{\varepsilon}}^p(t) \right\} \quad (11)$$

204 Since the residual stress rate field $\dot{\boldsymbol{\rho}}(t)$ is self-equilibrated and the strain rate $\dot{\boldsymbol{\varepsilon}}(t)$ is

205 kinematically admissible, the principle of virtual work states as follows:

$$206 \quad \int_V \delta \dot{\boldsymbol{\varepsilon}}^T(t) \cdot \dot{\boldsymbol{\rho}}(t) dV = 0 \quad (12)$$

207 where the superscript T denotes the symbol of transpose and $\delta \dot{\boldsymbol{\varepsilon}}(t)$ is the virtual strain rate.

208 Substituting Eqs. (10) and (11) into Eq. (12), we get

$$209 \quad \delta \dot{\mathbf{u}}^T(t) \cdot \left\{ \int_V \mathbf{B}^T \cdot \mathbf{D} \cdot \left[\mathbf{B} \cdot \dot{\mathbf{u}}(t) - \lambda \left[\dot{\boldsymbol{\varepsilon}}^E(t) + \dot{\boldsymbol{\varepsilon}}_\theta(t) \right] - \dot{\boldsymbol{\varepsilon}}^p(t) \right] dV \right\} = 0 \quad (13)$$

210 Since Eq. (13) holds for any virtual displacement rate $\delta \dot{\mathbf{u}}(t)$, the integral formula consisting

211 in the equation must vanish, i.e.

$$212 \quad \left(\int_V \mathbf{B}^T \cdot \mathbf{D} \cdot \mathbf{B} dV \right) \cdot \dot{\mathbf{u}}(t) = \lambda \int_V \mathbf{B}^T \cdot \mathbf{D} \cdot \left[\dot{\boldsymbol{\varepsilon}}^E(t) + \dot{\boldsymbol{\varepsilon}}_\theta(t) \right] dV + \int_V \mathbf{B}^T \cdot \mathbf{D} \cdot \dot{\boldsymbol{\varepsilon}}^p(t) dV \quad (14)$$

213 We replace the term $\mathbf{D} \cdot \dot{\boldsymbol{\varepsilon}}^p(t)$ with $\boldsymbol{\sigma}^C(t)$ which is named as the compensation stress

214 here, and substitute Eqs. (7) and (10) into Eqs. (14) and (11). Then Eqs. (14) and (11) become,

215 respectively

$$216 \quad \mathbf{K} \cdot \dot{\mathbf{u}}(t) = \lambda \int_V \mathbf{B}^T \cdot \dot{\boldsymbol{\sigma}}^E(t) dV + \lambda \int_V \mathbf{B}^T \cdot \mathbf{D} \cdot \dot{\boldsymbol{\varepsilon}}_\theta(t) dV + \int_V \mathbf{B}^T \cdot \boldsymbol{\sigma}^C(t) dV$$

$$\mathbf{K} = \int_V \mathbf{B}^T \cdot \mathbf{D} \cdot \mathbf{B} dV$$

$$217 \quad \dot{\boldsymbol{\rho}}(t) = \mathbf{D} \cdot \mathbf{B} \cdot \dot{\mathbf{u}}(t) - \lambda \dot{\boldsymbol{\sigma}}^E(t) - \lambda \mathbf{D} \cdot \dot{\boldsymbol{\varepsilon}}_\theta(t) - \boldsymbol{\sigma}^C(t) \quad (16)$$

218 where \mathbf{K} is the global stiffness matrix of the structure. Then the residual stress for

219 shakedown analysis is calculated by

$$220 \quad \boldsymbol{\rho}(t + \Delta t) = \boldsymbol{\rho}(t) + \int_t^{t+\Delta t} \dot{\boldsymbol{\rho}}(t) dt \quad (17)$$

221 For load vertex i , the total stresses at all the Gauss points in a body are calculated:

$$222 \quad \boldsymbol{\sigma}(t_i) = \lambda \boldsymbol{\sigma}^E(t_i) + \boldsymbol{\rho}(t_i) \quad (18)$$

223 It should be noted that t_i denotes the stress state of the body at the load vertex i . As illustrated

224 in Fig. 2, the total stress vector \overrightarrow{OC} ($\boldsymbol{\sigma}(t_i)$) is equal to the sum of the residual stress vector

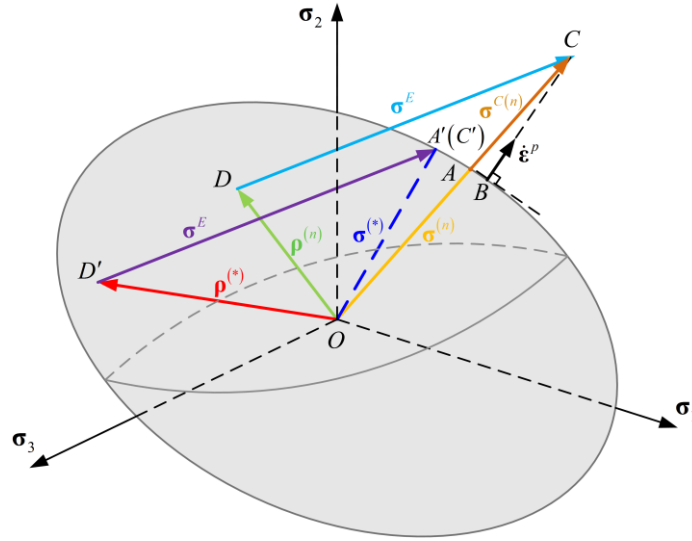
225 \overrightarrow{OD} ($\boldsymbol{\rho}(t_i)$) and the fictitious elastic stress vector \overrightarrow{DC} ($\lambda \boldsymbol{\sigma}^E(t_i)$), and the part in excess of

226 the von Mises yield surface is defined as the compensation stress vector \overrightarrow{AC} ($\boldsymbol{\sigma}^C(t_i)$) which

227 is calculated by the following formulae:

$$228 \quad \boldsymbol{\sigma}^C(t_i) = \xi(t_i) \cdot \boldsymbol{\sigma}(t_i), \quad \xi(t_i) = \begin{cases} \frac{\bar{\sigma}(t_i) - \sigma_y}{\bar{\sigma}(t_i)} & (\bar{\sigma}(t_i) > \sigma_y) \\ 0 & (\bar{\sigma}(t_i) \leq \sigma_y) \end{cases} \quad (19)$$

229 If we substitute Eq. (19) into (15), the nodal displacement rate $\dot{\mathbf{u}}(t_i)$ can be obtained by
 230 solving the equilibrium equations in Eq. (15). Then, a new residual stress field $\boldsymbol{\rho}(t_i)$ can be
 231 updated by Eq. (17).



232

233 **Fig. 2.** Von Mises yield surface and stress superposition schematic.

234 Because the equilibrium equations in Eq. (15) are established for every load vertex, it will
 235 require more time to solve these equilibrium equations with the increase of the number of
 236 vertices. Now, we superpose all the expressions (Eq. (20)) of residual stress rates over a load
 237 cycle.

$$238 \quad \begin{aligned} \dot{\boldsymbol{\rho}}(t_1) &= \mathbf{D} \cdot \mathbf{B} \cdot \dot{\mathbf{u}}(t_1) - \lambda \dot{\boldsymbol{\sigma}}^E(t_1) - \lambda \mathbf{D} \cdot \dot{\boldsymbol{\epsilon}}_\theta(t_1) - \boldsymbol{\sigma}^C(t_1) \\ \dot{\boldsymbol{\rho}}(t_2) &= \mathbf{D} \cdot \mathbf{B} \cdot \dot{\mathbf{u}}(t_2) - \lambda \dot{\boldsymbol{\sigma}}^E(t_2) - \lambda \mathbf{D} \cdot \dot{\boldsymbol{\epsilon}}_\theta(t_2) - \boldsymbol{\sigma}^C(t_2) \\ &\vdots \\ \dot{\boldsymbol{\rho}}(t_{NV}) &= \mathbf{D} \cdot \mathbf{B} \cdot \dot{\mathbf{u}}(t_{NV}) - \lambda \dot{\boldsymbol{\sigma}}^E(t_{NV}) - \lambda \mathbf{D} \cdot \dot{\boldsymbol{\epsilon}}_\theta(t_{NV}) - \boldsymbol{\sigma}^C(t_{NV}) \end{aligned} \quad (20)$$

239 Then the residual stress rates can be written as

$$240 \quad \begin{aligned} \dot{\boldsymbol{\rho}}(t^*) &= \mathbf{D} \cdot \mathbf{B} \cdot \dot{\mathbf{u}}(t^*) - \lambda \dot{\boldsymbol{\sigma}}^E(t^*) - \lambda \mathbf{D} \cdot \dot{\boldsymbol{\epsilon}}_\theta(t^*) - \boldsymbol{\sigma}^C(t^*) \\ \dot{\boldsymbol{\rho}}_0 &= \frac{1}{NV} \dot{\boldsymbol{\rho}}(t^*) \end{aligned} \quad (21)$$

241 where

$$\begin{aligned}
\dot{\boldsymbol{\rho}}(t^*) &= \dot{\boldsymbol{\rho}}(t_1) + \dot{\boldsymbol{\rho}}(t_2) + \cdots + \dot{\boldsymbol{\rho}}(t_{NV}) \\
\dot{\mathbf{u}}(t^*) &= \dot{\mathbf{u}}(t_1) + \dot{\mathbf{u}}(t_2) + \cdots + \dot{\mathbf{u}}(t_{NV}) \\
\dot{\boldsymbol{\sigma}}^E(t^*) &= \dot{\boldsymbol{\sigma}}^E(t_1) + \dot{\boldsymbol{\sigma}}^E(t_2) + \cdots + \dot{\boldsymbol{\sigma}}^E(t_{NV}) \\
\dot{\boldsymbol{\varepsilon}}_\theta(t^*) &= \dot{\boldsymbol{\varepsilon}}_\theta(t_1) + \dot{\boldsymbol{\varepsilon}}_\theta(t_2) + \cdots + \dot{\boldsymbol{\varepsilon}}_\theta(t_{NV}) \\
\boldsymbol{\sigma}^C(t^*) &= \boldsymbol{\sigma}^C(t_1) + \boldsymbol{\sigma}^C(t_2) + \cdots + \boldsymbol{\sigma}^C(t_{NV})
\end{aligned} \tag{22}$$

Here, $\dot{\boldsymbol{\rho}}_0$ is the updated residual stress rate of the structure for shakedown analysis, and NV denotes the number of vertices within a load cycle. By this way, the equilibrium equations in Eq. (15) just need to be solved only once for every load cycle.

The iterative procedure can be summarized as follows, for the iteration m :

(1) If $m=1$, the residual stress field $\boldsymbol{\rho}_0^{(1)}$ is initialized to zero. Calculate the total stresses $\boldsymbol{\sigma}^{(m)}(t_i)$ at all the Gauss points in a body for each load vertex i .

$$\boldsymbol{\sigma}^{(m)}(t_i) = \lambda^{(k)} \boldsymbol{\sigma}^E(t_i) + \boldsymbol{\rho}_0^{(m)}, \quad i = 1, 2, \dots, NV \tag{23}$$

(2) Check whether the total stress $\boldsymbol{\sigma}^{(m)}(t_i)$ at every Gauss point of the body exceeds the von Mises yield surface $f(\boldsymbol{\sigma})=0$ for the NV vertices of a load cycle, and calculate the corresponding compensation stress $\boldsymbol{\sigma}^{C(m)}(t_i)$.

(3) Solve the global equilibrium equations in Eq. (24) to obtain the nodal displacement rate $\dot{\mathbf{u}}^{(m+1)}(t^*)$ for next iteration. Then a new residual stress field $\boldsymbol{\rho}_0^{(m+1)}$ can be updated by Eqs. (25)-(27).

$$\mathbf{K} \cdot \dot{\mathbf{u}}^{(m+1)}(t^*) = \sum_{i=1}^{NV} \left\{ \lambda^{(k)} \int_V \mathbf{B}^T \cdot [\dot{\boldsymbol{\sigma}}^E(t_i) + \mathbf{D} \cdot \dot{\boldsymbol{\varepsilon}}_\theta(t_i)] dV + \int_V \mathbf{B}^T \cdot \boldsymbol{\sigma}^{C(m)}(t_i) dV \right\} \tag{24}$$

$$\dot{\boldsymbol{\rho}}(t^*) = \mathbf{D} \cdot \mathbf{B} \cdot \dot{\mathbf{u}}^{(m+1)}(t^*) - \sum_{i=1}^{NV} \left[\lambda^{(k)} \dot{\boldsymbol{\sigma}}^E(t_i) + \lambda^{(k)} \mathbf{D} \cdot \dot{\boldsymbol{\varepsilon}}_\theta(t_i) + \boldsymbol{\sigma}^C(t_i) \right] \tag{25}$$

$$\dot{\boldsymbol{\rho}}_0 = \frac{1}{NV} \dot{\boldsymbol{\rho}}(t^*) \tag{26}$$

$$\boldsymbol{\rho}_0^{(m+1)} = \boldsymbol{\rho}_0^{(m)} + \int_t^{t+t^*} \dot{\boldsymbol{\rho}}_0 dt \tag{27}$$

(4) Check the change of the value of the compensation stress $\boldsymbol{\sigma}^{C(m)}(t_i)$, and repeat the steps 1-3 till the iterative process converges.

262 It is worth noting that the convergence of the compensation stress $\sigma^{C(m)}(t_i)$ is equivalent
263 to Condition (28)

$$264 \quad \left| \xi^{(m+1)}(t_i) - \xi^{(m)}(t_i) \right| \leq tol1 \quad (28)$$

265 where *tol1* is a tolerance parameter which dynamically reduces according to the value of
266 $\xi^{(m)}(t_i)$.

267 The above procedure provides an efficient strategy to search the statically admissible
268 constant residual stress field for shakedown analysis. Each iteration will generate a new
269 self-equilibrated residual stress field. For every vertex of a load cycle, the conditions of the
270 static shakedown theorem are examined. If the conditions of the static shakedown theorem are
271 violated, the compensation stress $\sigma^C(t)$ will be added to adjust the total stress to the yield
272 surface, and then a new self-equilibrated residual stress field is updated again. When the
273 iterative process converges, the residual stress field no longer changes and the evolution of
274 compensation stress $\sigma^C(t)$ is also obtained. Thus, the compensation stress can be
275 considered as a symbol for estimating whether the structure shakes down, i.e., whether all the
276 conditions of the static shakedown theorem are satisfied. If the compensation stresses at all
277 Gauss points of the body for every vertex of a load cycle vanish, the structure shakes down.

278 **4 Numerical procedure of the SCM for shakedown analysis**

279 In section 3, the SCM presents an approach to calculating constant residual stress field for
280 shakedown analysis and provides a symbol to estimate whether the structure made up of the
281 elastic-perfectly plastic material shakes down. In this section, an iterative procedure well
282 suitable for shakedown analysis is proposed.

283 **4.1 Evaluation of an initial load multiplier**

284 The numerical procedure starts with an initial load multiplier λ^{ini} and the fictitious
285 elastic stresses $\sigma^E(t_i)$. The fictitious elastic stresses $\sigma^E(t_i)$ can be obtained via some
286 elastic finite element analyses. An appropriate initial load multiplier λ^{ini} can be calculated

287 by

$$288 \quad \lambda^{\text{ini}} = \frac{\int_V \left(\sigma_y \sum_{i=1}^{NV} \bar{\varepsilon}_i \right) dV}{\int_V \left(\sum_{i=1}^{NV} \boldsymbol{\sigma}^E(t_i) \cdot \boldsymbol{\varepsilon}^E(t_i) \right) dV} \quad (29)$$

289 where $\boldsymbol{\varepsilon}^E(t_i)$ is the elastic strain corresponding to the fictitious elastic stress $\boldsymbol{\sigma}^E(t_i)$, and $\bar{\varepsilon}_i$
 290 is the effective strain of $\boldsymbol{\varepsilon}^E(t_i)$. Then the value of the initial load multiplier must be bigger
 291 than that of the shakedown limit.

292 4.2 Iterative procedure for shakedown analysis

293 The numerical procedure is made up of two iteration loops. The inner one controlled by
 294 iteration m is used to obtain the compensation stress $\boldsymbol{\sigma}^C(t_i)$ at every load vertex and the
 295 constant residual stress field for shakedown analysis. The outer one controlled by iteration k is
 296 used to update the shakedown load multiplier. The iterative steps are then followed, for the
 297 outer iteration k :

- 298 (1) Complete all of the steps in the inner loop, which is summarized in Section 3.
 299 (2) Calculate the maximum value of the variable $\xi^{(m+1)}(t_i)$ at all the Gauss points for all
 300 load vertices at the end of load cycle, that is

$$301 \quad \xi_{\max}^{(k+1)} = \max \left(\xi^{(m+1)}(t_i) \right) \quad (30)$$

- 302 (3) The following judgments are examined:

$$303 \quad \frac{\xi_{\max}^{(k+1)}}{\xi_{\max}^{(k)}} \leq \text{tol2}, \text{ and } \omega > 0.1 \quad (31)$$

304 where tol2 usually takes 0.1~0.2; the initial value of $\xi_{\max}^{(1)}$ is 1.0; and ω is a convergence
 305 parameter with an initial value 0.1~0.5. If Condition (31) holds, the load multiplier is
 306 modified by

$$307 \quad \lambda^{(k+1)} = \frac{\lambda^{(k)} \left(1 - \frac{\omega}{2} \cdot \xi_{\max}^{(k+1)} \right)}{\left(1 - \omega \cdot \xi_{\max}^{(k+1)} \right)} \quad (32)$$

308 and then the convergence parameter ω is halved:

$$309 \quad \omega = \frac{\omega}{2} \quad (33)$$

310 otherwise, a new load multiplier is calculated by the following expression:

$$311 \quad \lambda^{(k+1)} = \lambda^{(k)} \left(1 - \omega \cdot \xi_{\max}^{(k+1)} \right) \quad (34)$$

312 where $\lambda^{(k)}$ is the previous load multiplier; and $\lambda^{(k+1)}$ is the updated load multiplier.

313 (4) A desired tolerance $tol3$ is given to estimate whether $\xi_{\max}^{(k+1)}$ approaches to zero or not

$$314 \quad \xi_{\max}^{(k+1)} \leq tol3 \quad (35)$$

315 (5) Repeat the steps 1~4. If condition (35) is satisfied, the calculated load multiplier becomes
316 the shakedown limit multiplier λ_{sh} , i.e.

$$317 \quad \lambda^{(k+1)} = \lambda_{sh} \quad (36)$$

318 otherwise, a new outer iteration starts.

319 **4.3 Convergence and accuracy considerations**

320 A robust and effective iterative control technique and some tolerance parameters are
321 adopted in the numerical procedure to ensure the calculation accuracy and efficiency of the
322 method. Beginning with an initial load multiplier above the shakedown limit, the novel SCM
323 procedure for the shakedown analysis will generate a series of descending load multipliers
324 that converge to the shakedown limit.

325 The tolerance parameter $tol1$ used to stop the inner loop, is the key factor to balance the
326 accuracy and efficiency of the algorithm. Small value of $tol1$ that represents the strict
327 convergence criteria will lead to a more sophisticated calculation of constant residual stress
328 field for shakedown analysis. The calculated shakedown limit multiplier is mainly determined
329 by the finally convergent solution that satisfies the entire conditions of the static shakedown
330 theorem, and has few relations with the solution in the intermediate process where the
331 conditions of the static shakedown theorem are not satisfied. Therefore, the dynamically
332 varying values of $tol1$, which is large in the beginning of the iterative procedure and becomes
333 smaller with the approaching of load multiplier to shakedown limit multiplier, are adopted to

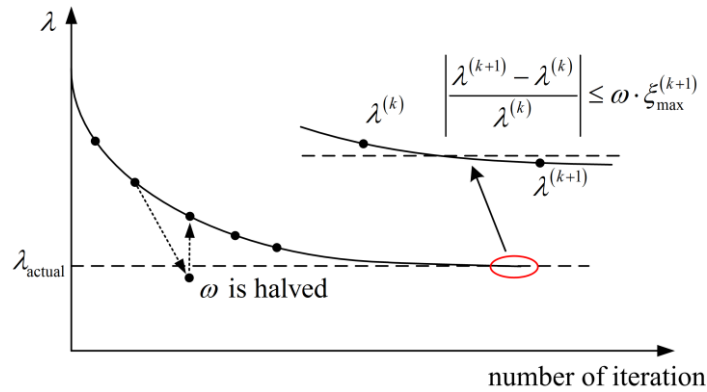
334 improve the speed of convergence. A final value of $tol1=10^{-4}$ turns out to be enough for a
 335 good calculation accuracy.

336 An initial convergence parameter $\omega=0.5$ does not prohibit the load multiplier from
 337 overshooting below the target solution at shakedown limit, and hence the numerical scheme
 338 shown in Eqs. (31)-(33) is followed to deal with this problem. Then even though the
 339 overshooting dose still occur, its value becomes negligible. If Condition (31) is satisfied, the
 340 calculated load multiplier will increase till its value exceeds the shakedown limit, and then the
 341 iterative procedure goes on. A typical convergence procedure of the SCM for shakedown
 342 analysis is illustrated in Fig. 3.

343 Since that, the adopted shakedown criterion is based on the static shakedown theorem and
 344 the entire conditions of the theorem are satisfied when the iterative procedure converges, the
 345 calculated shakedown limit multiplier will be a lower bound to the actual shakedown solution.
 346 In fact, the criterion in Eq. (35) is equivalent to the following form:

$$347 \quad \left| \frac{\lambda^{(k+1)} - \lambda^{(k)}}{\lambda^{(k)}} \right| \leq \omega \cdot \xi_{\max}^{(k+1)} \quad (37)$$

348 Because the value of ω is no more than 0.5, the relative error of the calculated shakedown
 349 limit multiplier is no more than 0.1%.



350

351 **Fig. 3.** Typical convergence procedure of the SCM for shakedown analysis.

352 5 Numerical applications

353 In this section, three different numerical examples of shakedown analysis for structures
 354 under mechanical and thermal loads that vary within multi-dimensional loading domain are

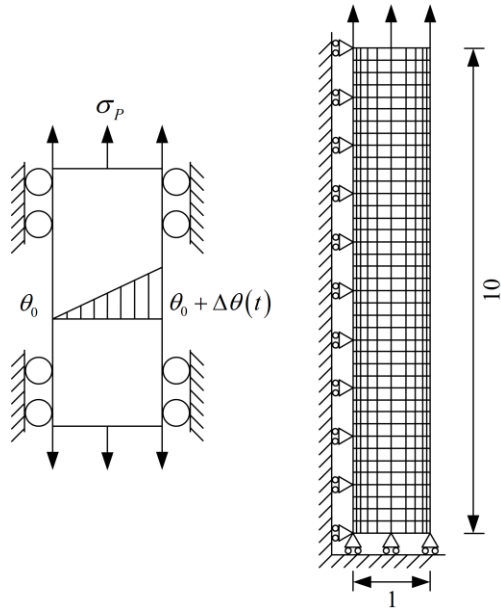
355 considered. The presented algorithm is implemented into the commercial finite element
356 software ABAQUS [47] via user subroutine UMAT and is used to calculate the shakedown
357 limits of these structures.

358 All the structures are made up of homogeneous, isotropic and elastic-perfectly plastic
359 material with von Mises yield surface. The material parameters are assumed independent of
360 the applied temperature and constant with time. All the calculations are carried out on the
361 personal computer with 16GB RAM and Intel Core i7 at 3.39GHz.

362 5.1 Bree problem

363 The first example is the Bree problem [37, 40, 46, 48, 49], which is a common benchmark
364 example of shakedown analysis for structures under mechanical and thermal loads. As
365 illustrated in Fig. 4, the thin plate is subjected to a tension σ_p and a temperature difference
366 $\Delta\theta(t)$ that is linearly distributed along the width of the plate, and the deformation due to the
367 thermal gradient is restrained by boundary constraints. The tension σ_p and the temperature
368 difference $\Delta\theta(t)$ may vary in three different loading paths, as shown in Fig. 5. The finite
369 element model of the plate consists of 630 8-node quadratic plane stress elements (ABAQUS
370 CPS8) with 3×3 Gauss integration points. The material properties of the plate are given in
371 Table 1.

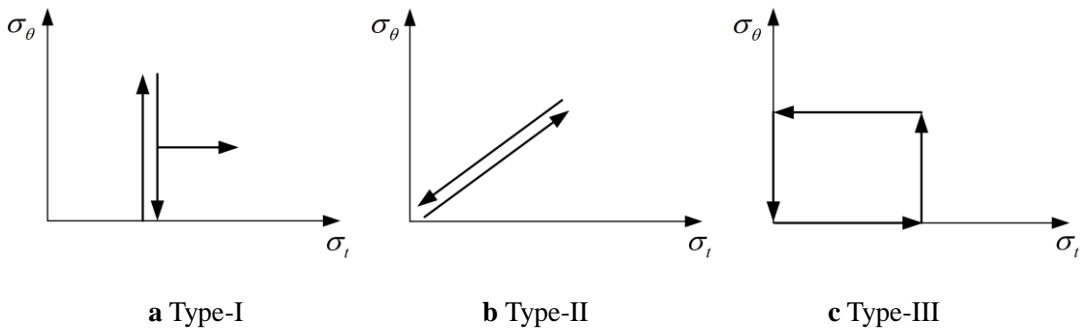
372 The plane stress Bree cases considering two loading paths (Fig. 5a and b) have been
373 studied numerically and analytically by some authors [40, 49], and the two loading paths
374 correspond to two types (Type-I and Type-II) of the Bree problem. Here, three different
375 loading paths are considered for the purposes of comparison and verification.



376

377

Fig. 4. Geometry and finite element model for the Bree problem.



378

379

380

Fig. 5. Three loading paths for the Bree problem.

381

Table 1 Material properties of the thin plate.

Young's modulus E	Poisson's ratio ν	Yield stress ..	Coefficient of thermal expansion α
208 GPa	0.3	360 MPa	$5 \times 10^{-5} / ^\circ\text{C}$

382

5.1.1 Type-I

383

384

385

386

The first type (Type-I) is the classic Bree problem, where the thermal load is cyclic and the mechanical load is constant. The analytical solution of the classic Bree problem for von Mises yield criterion has been provided by Bree [48], and the shakedown boundary can be determined by two straight-line segments (Fig. 6), that is

387

$$\frac{\sigma_{\theta}}{\sigma_y} = 2 \quad \forall 0 \leq \frac{\sigma_p}{\sigma_y} \leq \frac{1}{2}$$

$$\frac{\sigma_p}{\sigma_y} + \frac{1}{4} \frac{\sigma_{\theta}}{\sigma_y} = 1 \quad \forall \frac{1}{2} < \frac{\sigma_p}{\sigma_y} \leq 1$$

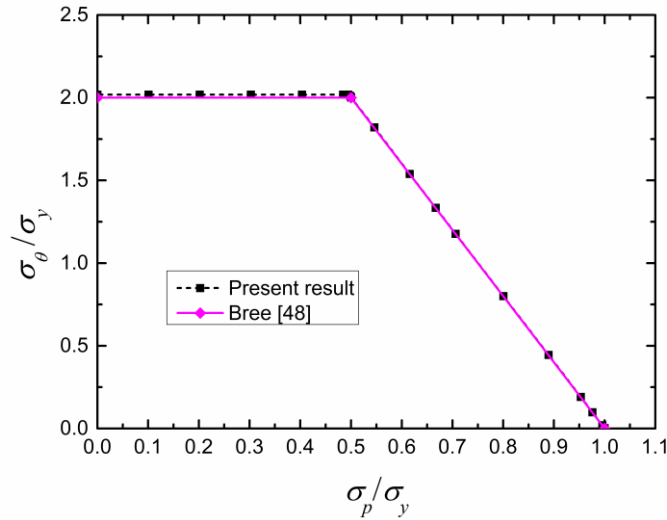
388

389

(38)

388 where σ_{θ} is the maximum thermal elastic stress due to the fluctuating temperature
 389 difference $\Delta\theta(t)$.

390 The SCM is used to calculate shakedown limits of the plate under various ratios of the
 391 constant tension and the fluctuating temperature difference. As a result, the corresponding
 392 numerical results are displayed in Fig. 6, where the tension σ_p and the maximum thermal
 393 stress σ_{θ} are normalized by the uniaxial yield stress.



394

395 **Fig. 6.** Shakedown limits calculated by the SCM and its comparison with the analytical
 396 solution by Bree [48] for Type-I Bree problem.

397 It can be seen from Fig. 6 that the numerical results by the SCM are in good agreement
 398 with the analytical solution, apart from some slight differences in the segment where σ_p / σ_y
 399 ranges from 0.0 to 0.5. This segment just corresponds to the alternating plasticity region of
 400 shakedown boundary. The slight differences can be explained with the failure mechanism of
 401 the structure when it fails to shake down. If the alternating plasticity mechanism is decisive
 402 for shakedown, the maximum stress point in the structure will dominate the shakedown limit.
 403 The maximum stress points are located on the edges of the plate in this case; however, there is

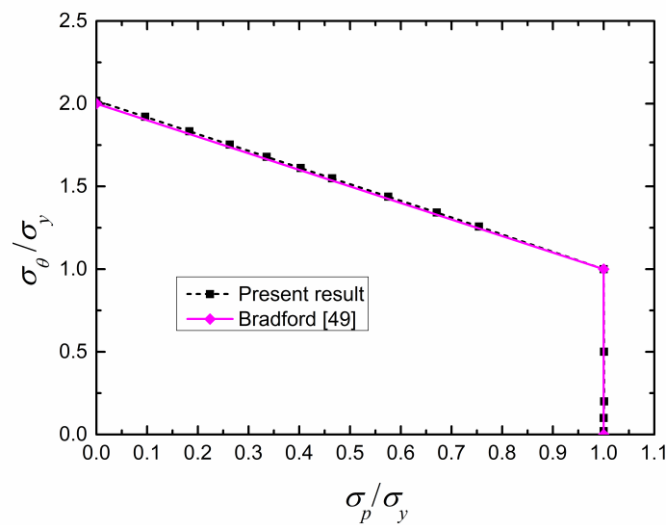
404 no Gauss points on them. The stress via the finite element calculation will be slightly lower
 405 than the actual stress at the edge. Thus, the computed shakedown limit by the SCM is slightly
 406 higher than the analytical solution in the alternating plasticity region. This merely
 407 demonstrates that the difference is due to the finite element solution. If the finite element
 408 discretization is finer, we will obtain a nearer solution to the exact one.

409 5.1.2 Type-II

410 The second type (Type-II) is the modified Bree problem, where the thermal load and the
 411 mechanical load vary proportionally. The analytical solution of the Type-II Bree problem for
 412 von Mises yield criterion has been obtained by Bradford [49], and the shakedown boundary
 413 shown in Fig. 7 can be determined by

$$\begin{aligned}
 \frac{\sigma_{\theta}}{\sigma_y} + \frac{\sigma_p}{\sigma_y} &= 2 & \forall 1 \leq \frac{\sigma_{\theta}}{\sigma_y} \leq 2 \\
 \frac{\sigma_p}{\sigma_y} &= 1 & \forall 0 \leq \frac{\sigma_{\theta}}{\sigma_y} \leq 1
 \end{aligned}
 \tag{39}$$

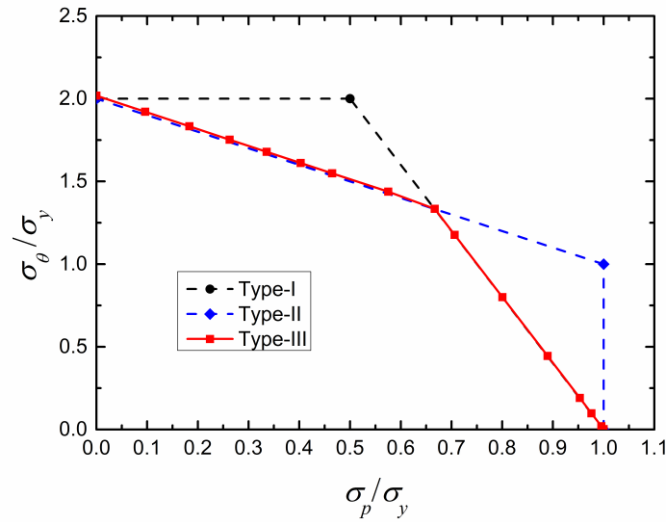
415 The SCM is used to calculate the shakedown boundary of the Type-II problem, and the
 416 corresponding numerical results are displayed in Fig. 7. That the maximum relative error
 417 between the numerical results and the analytical solutions is no more than 0.9% demonstrates
 418 the good accuracy of the SCM.



419
 420 **Fig. 7.** Shakedown limits calculated by the SCM and its comparison with the analytical
 421 solution by Bradford [49] for Type-II Bree problem.

422 5.1.3 Type-III

423 The third type (Type-III) is another modified Bree problem, where the thermal load and
 424 the mechanical load vary independently. Fig. 8 shows the numerical results of the shakedown
 425 analysis by the SCM.

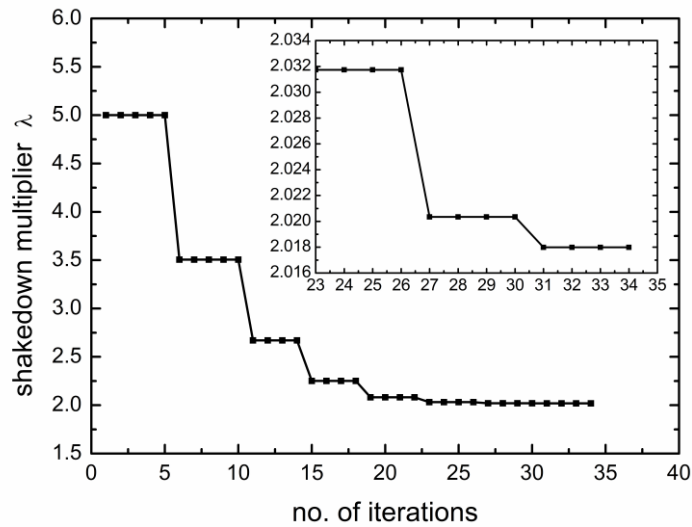


426

427 **Fig. 8.** Shakedown limits calculated by the SCM for Type-III Bree problem.

428 It can be seen from Fig. 8 that the shakedown boundary of the Type-III Bree problem is
 429 the lower envelope of the shakedown boundaries of the Type-I Bree problem and the Type-II
 430 Bree problem. Therefore, a more stringent shakedown domain can be obtained when the
 431 mechanical and thermal loads vary independently in a rectangle loading domain. Thus, the
 432 loading condition of structural components must be assessed carefully in practical engineering
 433 design.

434 For the three types of the Bree problems above, the procedures of the SCM for shakedown
 435 analysis all present good convergence and the numerical results are in good agreement with
 436 these analytical solutions. A typical iterative convergence process of the shakedown multiplier
 437 λ for the load combination $\sigma_p = 0$ is depicted in Fig. 9, where the horizontal line segment
 438 indicates that the procedure of the SCM is being carried out in its inner iterative loop and the
 439 jump point indicates the procedure of the SCM is being carried out in its outer iterative loop.
 440 As a result, the y-axial component residual stress field of the plate is displayed in Fig. 10
 441 when the shakedown limit reaches.

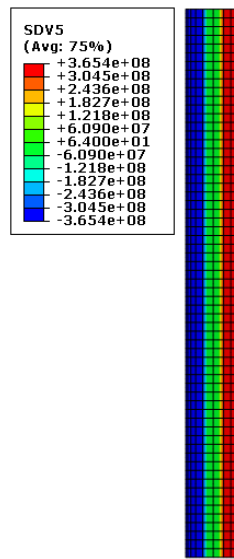


442

443 **Fig. 9.** A typical iterative convergence process of the shakedown multiplier for the Bree

444

problem.



445

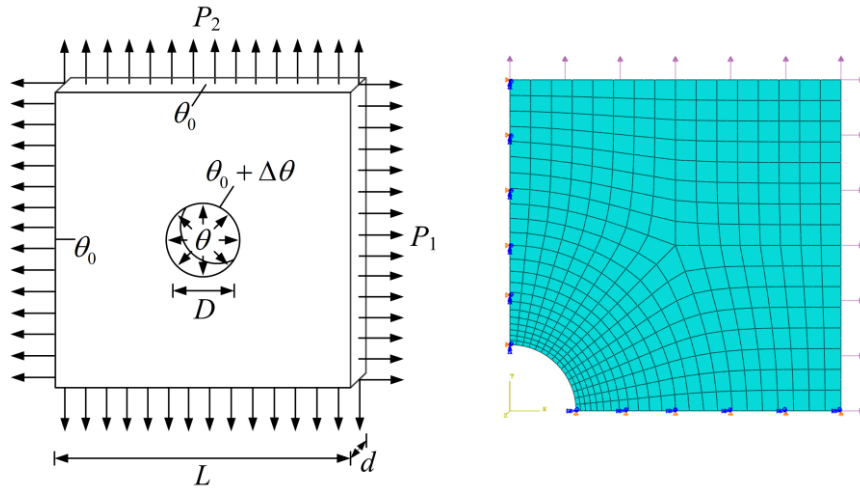
446

Fig. 10. Y-axial component residual stress field of the plate.

447 5.2 Square plate with a central circular hole

448 Tube sheets are usually used as supporting elements in heat exchangers and boilers. When
 449 heated fluid passes through the tubes, the tube sheets undergo temperature difference, which
 450 may cause thermal stresses in their bodies. The representative cell including a square plate
 451 with a central circular hole (Fig. 11) is established to investigate the load-carrying capability
 452 of tube sheets under variable mechanical and thermal loads.

453 Due to the symmetry of the structure and the loading, only one quarter of the holed plate
 454 is considered. The geometry of the structure and its quarter finite element model are shown in
 455 Fig. 11. The ratio between the diameter D of the circular hole and the length L of the square
 456 plate is 0.2. The ratio between the thickness d of the plate and its length L is 0.05. The mesh
 457 discretization consists of 432 8-node quadratic plane stress elements (ABAQUS CPS8) with
 458 3×3 Gauss integration points. The material properties of the plate are the same as those given
 459 in Table 1.



460
 461

Fig. 11. Geometry of the holed plate and its quarter finite element model.

462 The plate is subjected to three loads that consist of a temperature difference $\Delta\theta(t)$
 463 between the edge of the hole and the outer edge of the plate, and two uniform normal
 464 tractions P_1 and P_2 at the vertical edge and the horizontal edge of the plate respectively. For
 465 the convenience of comparison, the variation of the temperature with radius r is assumed the
 466 same distribution as in [39, 46]:

$$467 \quad \theta = \theta_0 + \Delta\theta \frac{\ln\left(\frac{5D}{2r}\right)}{\ln(5)} \quad (40)$$

468 which is an approximation to the temperature field corresponding to $\theta = \theta_0 + \Delta\theta$ at the edge
 469 of the hole and $\theta = \theta_0$ around the outer edge of the plate.

470 For the calculations of different initial elastic stress fields, $P_1^* = P_2^* = 360\text{MPa}$, $\theta_0 = 0$
 471 and $\Delta\theta^* = 90.2^\circ\text{C}$ have been adopted. The maximum von Mises stress at the edge of the
 472 holed plate due to the thermal load is σ_θ . In order to test and verify the reliability of the

473 proposed procedure for shakedown analysis of the plate under multiple mechanical and
 474 thermal loads, three different loading conditions have been considered here.

475 (1) Case I

476 We consider that the three loads vary independently in the following ranges:

$$\begin{aligned}
 &0 \leq P_1 \leq \mu_1 P_1^* \\
 477 \quad &0 \leq P_2 \leq \mu_2 P_2^* \\
 &0 \leq \Delta\theta \leq \mu_3 \Delta\theta^*
 \end{aligned} \tag{41}$$

478 Then the loading domain becomes a cuboid in the space of load parameters, as shown in [Fig.](#)
 479 [12a](#). Considering the different ratios among μ_1 , μ_2 and μ_3 , 111 load combinations in the
 480 three-dimensional loading space are chosen for shakedown analysis of the plate, as illustrated
 481 in [Fig. 12b](#).

482 (2) Case II

483 Here we consider that the mechanical load P_1 keeps constant, and the mechanical load P_2
 484 and the thermal load vary independently, that is

$$\begin{aligned}
 &P_1 = \mu_1 P_1^* \\
 485 \quad &0 \leq P_2 \leq \mu_2 P_2^* \\
 &0 \leq \Delta\theta \leq \mu_3 \Delta\theta^*
 \end{aligned} \tag{42}$$

486 Then the loading domain becomes a plane in the space of load parameters, as shown in [Fig.](#)
 487 [12c](#). In order to depict the shakedown domain clearly, 205 load combinations in the
 488 three-dimensional loading space are chosen for shakedown analysis of the plate, as illustrated
 489 in [Fig. 12d](#). It is worth noting that the blue line plotted in [Fig. 12d](#) denotes these load
 490 combinations of $\mu_2/\mu_1=0.761$.

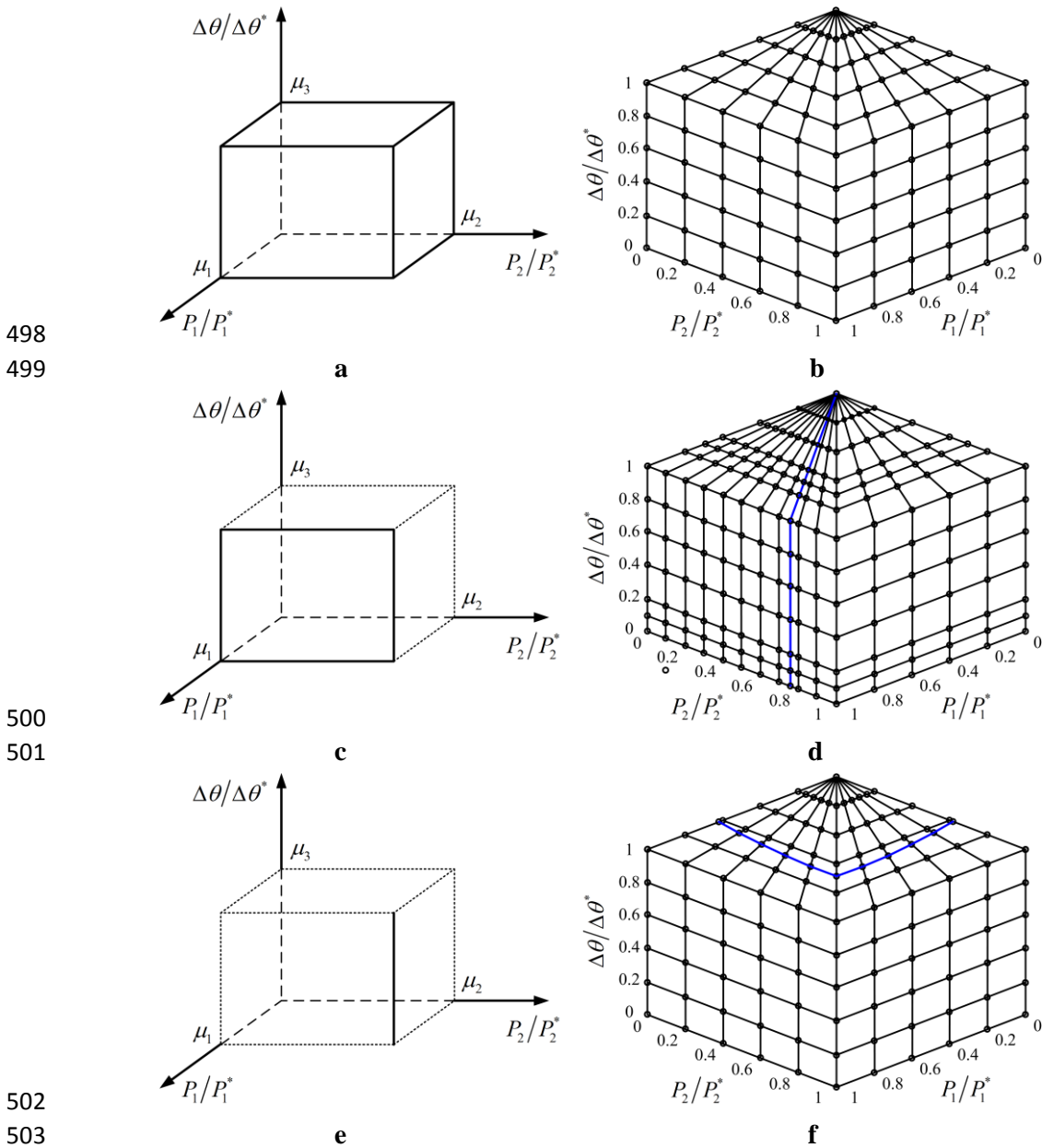
491 (3) Case III

492 Now we consider that the mechanical loads P_1 and P_2 keep constant, and the thermal load
 493 varies, that is

$$\begin{aligned}
 &P_1 = \mu_1 P_1^* \\
 494 \quad &P_2 = \mu_2 P_2^* \\
 &0 \leq \Delta\theta \leq \mu_3 \Delta\theta^*
 \end{aligned} \tag{43}$$

495 Then the loading domain becomes a line in the space of load parameters, as shown in [Fig. 12e](#).
 496 122 load combinations in the three-dimensional loading space are chosen for shakedown

497 analysis of the plate, as illustrated in Fig. 12f.



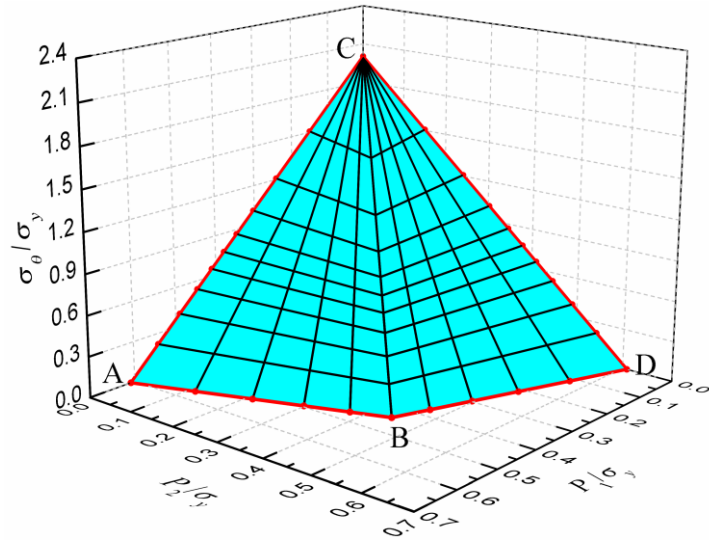
504 **Fig. 12.** Loading domain and computed load combinations in loading space.

505 The proposed algorithm is adopted to calculate the shakedown limits of the plate for the
 506 three cases. Fig. 13a, b and c show the three-dimensional shakedown domains of the plate for
 507 case I, case II and case III, respectively.

508 From Fig. 13a, one can observe that the 111 shakedown limit points are located in two
 509 intersecting planes, i.e., the plane A-B-C and the plane B-C-D. It is worth noting that the
 510 shakedown limit points in these two planes are both dominated by alternating plasticity
 511 mechanism. From Fig. 13b, it can be seen that the shakedown boundaries consist of the plane

512 B-C-D-E and the surface A-B-E, and that the shakedown domain expands comparing to that
513 in Fig. 13a. Moreover, the blue line B-D in Fig. 13b denotes the shakedown limits
514 corresponding to the load combinations of $\mu_2/\mu_1=0.761$, which are plotted as blue line in
515 Fig. 12d. It is worth noting that the shakedown limit points in the plane B-C-D-E are
516 dominated by alternating plasticity mechanism, and the points in the surface A-B-E are
517 dominated by ratcheting mechanism. From Fig. 13c, one can observe that the shakedown
518 boundaries consist of two surfaces A-B-E-D, B-C-F-E and the plane D-E-F-G, and the
519 shakedown domain further expands comparing to that in above two cases. It should be noted
520 that the shakedown limit points in the plane D-E-F-G are dominated by alternating plasticity
521 mechanism, and the points in both the surface A-B-E-D and the surface B-C-F-E are
522 dominated by ratcheting mechanism.

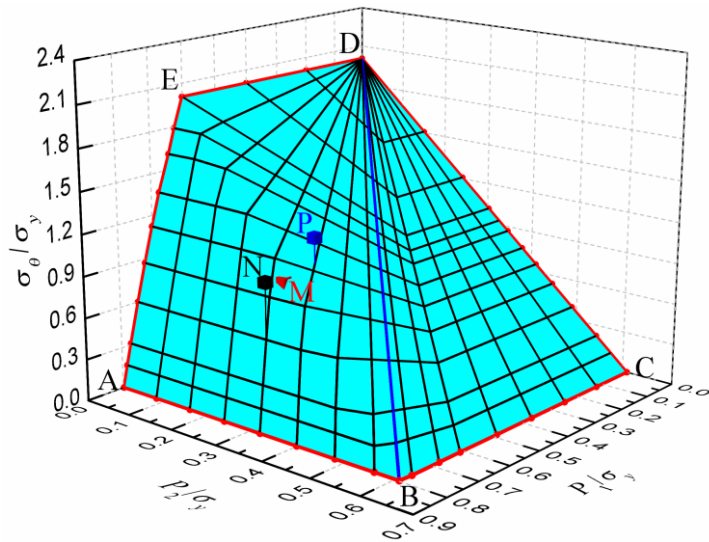
523 In order to verify the failure mechanism that dominates the shakedown boundaries of the
524 plate for different cases, several individual step-by-step incremental elastic-plastic
525 calculations are conducted, as depicted by the red, black and blue markers with capital letters
526 *M*, *N* and *P* in Fig. 13b and c. In both Fig. 13b and Fig. 13c, the load combination marked
527 with red “*M*” indicates shakedown behavior, while the load combination marked with black
528 “*N*” indicates alternating plasticity behavior and the red load combination marked with blue
529 “*P*” illustrates ratcheting behavior. As results, details relating to the effective plastic strains
530 over the first 15 load cycles at a Gauss point of the plate from the load combinations *M*, *N* and
531 *P* (Fig. 13b) are displayed in Fig. 14. Fig. 15 shows the effective plastic strains over the first
532 30 load cycles at a Gauss point of the plate from the three load combinations *M*, *N* and *P* (Fig.
533 13c). These results illustrate that the three load combinations *M*, *N* and *P* depicted in both Fig.
534 13b and Fig. 13c exhibit shakedown, alternating plasticity and ratcheting behavior,
535 respectively. The results from step-by-step incremental elastic-plastic analysis clearly reveal
536 the different failure mechanisms of the plate under various load combinations.



a for case I

537

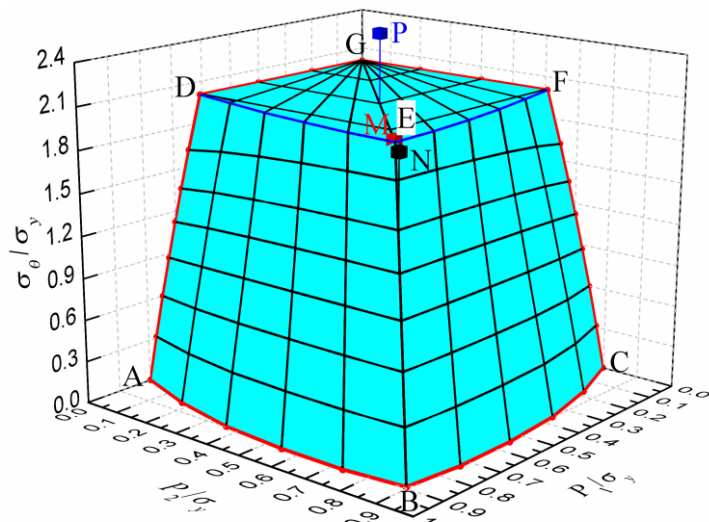
538



b for case II

539

540



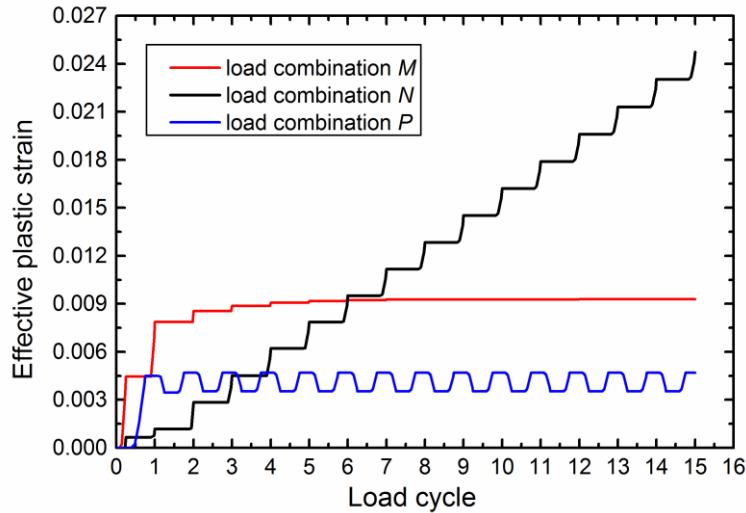
c for case III

541

542

543

Fig. 13. Shakedown domain of the plate in three-dimensional loading space.

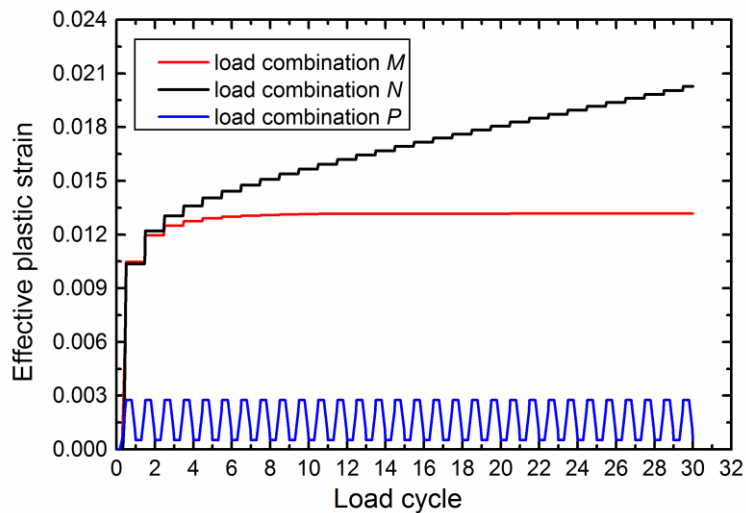


544

545 **Fig. 14.** Effective plastic strains over the first 15 load cycles at a Gauss point of the plate from

546

load combinations M , N and P for case II.



547

548 **Fig. 15.** Effective plastic strains over the first 30 load cycles at a Gauss point of the plate from

549

load combinations M , N and P for case III.

550 To describe quantitatively these shakedown domains of the plate, numerical results of
 551 shakedown analysis for some typical computed load combinations are given in Table 2. It is
 552 worth noting that these calculated shakedown limits are marked with capital letters in Fig. 13.

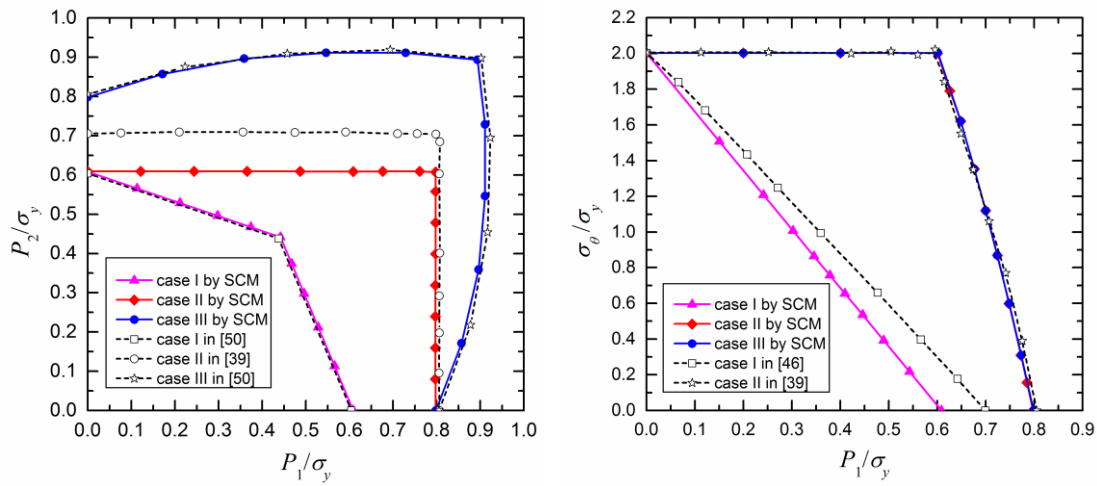
553 Assuming that one of the loads is equal to zero, the three-dimensional loading space
 554 degenerates into the two-dimensional loading space. Then the shakedown limit points will be
 555 presented as two-dimensional plot. Fig. 16a shows the shakedown domains of the plate in
 556 two-dimensional loading space when the thermal load vanishes for the three cases considered
 557 above. Fig. 16b shows the shakedown domains of the plate in two-dimensional loading space

558 when the mechanical load P_2 vanishes for the three cases considered above.

559 **Table 2** Numerical results of shakedown analysis in three-dimensional loading space.

Computed load combination	Shakedown limit (P_1/σ_y , P_2/σ_y , σ_θ/σ_y)		
	Case I	Case II	Case III
A	(0.609, 0, 0)	(0.798, 0, 0)	(0.798, 0, 0)
B	(0.442, 0.442, 0)	(0.798, 0.608, 0)	(0.894, 0.894, 0)
C	(0, 0, 2.002)	(0, 0.609, 0)	(0, 0.798, 0)
D	(0, 0.609, 0)	(0, 0, 2.002)	(0.608, 0, 2.002)
E	----	(0.608, 0, 2.002)	(0.685, 0.685, 2.002)
F	----	----	(0, 0.608, 2.002)
G	----	----	(0, 0, 2.002)

560



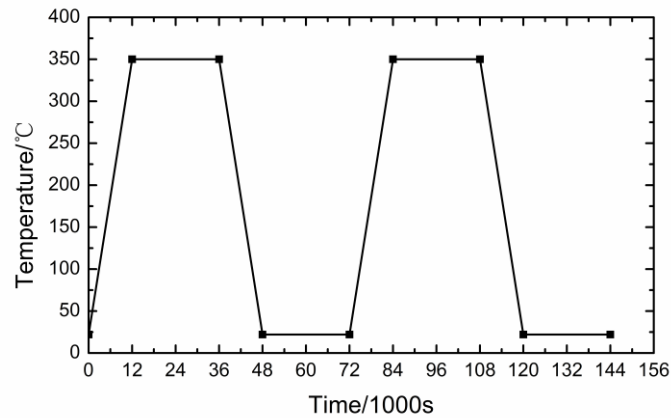
561

562 **a** thermal load vanishes

b mechanical load P_2 vanishes

563 **Fig. 16.** Shakedown domains of the plate in two-dimensional loading space.

564 As a typical example, the shakedown analysis of the holed plate under two loads has been
 565 studied by several authors [28, 30, 39, 46, 50]. For the comparison purpose, some results from
 566 [39, 46, 50] are plotted in Fig. 16 additionally. From Fig. 16a, we can observe that the present
 567 results are in good agreement with the solutions from [50] but have some differences with
 568 these from [39]. It should be stated that the discrepancy of the shakedown limits between our
 569 results and these from [39] is mainly due to the different mesh discretization. From Fig. 16b,
 570 we can observe that the present results are in good agreement with these from [39] but have
 571 some differences with these from [46]. The slight discrepancy of the shakedown limits

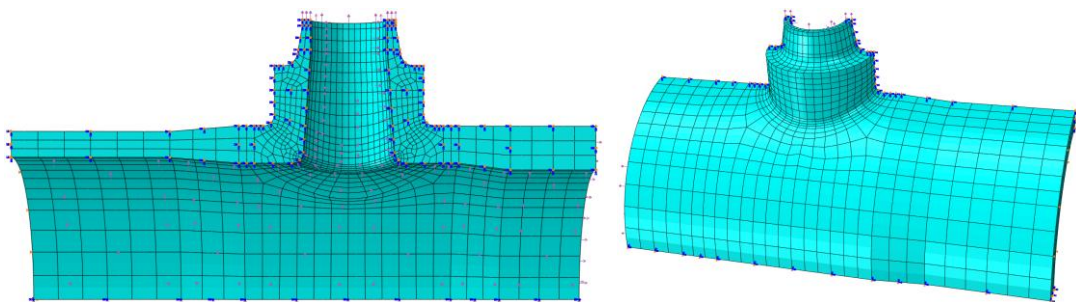


589

590 **Fig. 18.** Temperature history on the inside surface of the vessel and the nozzles.

591 Considering the symmetry of the structure and the loading, only one quarter of the thick
 592 vessel with nozzles is established. Fig. 19 shows the finite element model of the structure,
 593 where the symmetric boundary conditions are used and the forces acting on the ends of the
 594 vessel and nozzles are replaced with the equivalent uniformly distributed tensions to consider
 595 closed end condition. In order to optimize the efficiency and accuracy of the calculation, the
 596 finite element meshes around the stress concentration areas are refined properly. The mesh
 597 discretization consists of 3358 elements and 16655 nodes. In calculations, the 20-node
 598 quadratic brick elements (ABAQUS C3D20D) are used for the determination of the
 599 temperature distribution and the 20-node quadratic brick elements with reduced integration
 600 (ABAQUS C3D20R) are used for the structural stress analysis.

601 The material properties of the vessel with nozzles are given in Table 3.



602

603 **Fig. 19.** Finite element model of the thick vessel with nozzles.

604

605

606

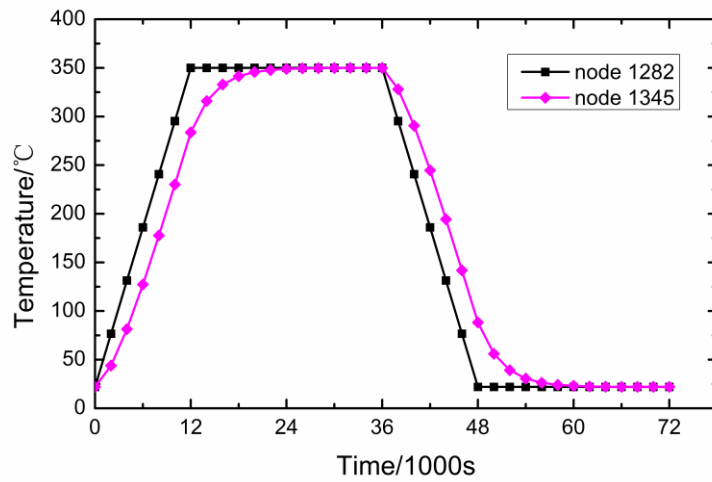
Table 3 Material properties of the thick vessel with nozzles.

Young's modulus E	2.1×10^5 MPa
Poisson's ratio ν	0.3
Yield stress σ_y	200 MPa
Density ρ	8100 kg/m ³
Thermal conductivity	18 W/(m°C)
Specific heat capacity	430 J/(kg°C)
Coefficient of thermal expansion α	1.8×10^{-5}

607

608 *5.3.1 Heat transfer analysis and elastic stress calculation*

609 First, the transient heat transfer analysis is carried out to calculate the temperature field
610 history of the entire body. As a result, temperature histories of nodes 1282 and 1345 are
611 shown in Fig. 20, each of which represents a node on the inside or the outside surface of the
612 vessel respectively. Then the structural stress analysis is followed to calculate the thermal
613 elastic stress field and the mechanical elastic stress field. The dangerous moments for the
614 vessel with nozzles under thermal load are at 12000 s and 48000 s, which are just the final
615 moments of the start-up and the shutdown respectively. Fig. 21a and b show the temperature
616 field distributions of the vessel with nozzles at 12000 s and 48000 s, respectively. The
617 corresponding von Mises elastic stress fields are displayed in Fig. 22a and b, respectively. It
618 should be noted that although the distributions of von Mises elastic stress field in Fig. 22a and
619 b are the same, the directions of stress fields at 12000 s and 48000 s are opposite, and thus the
620 structure suffers from the maximum stress range between the two moments. The von Mises
621 elastic stress field of the vessel with nozzles under internal pressure is shown in Fig. 23.



622

623

Fig. 20. Temperature histories of nodes 1282 and 1345.

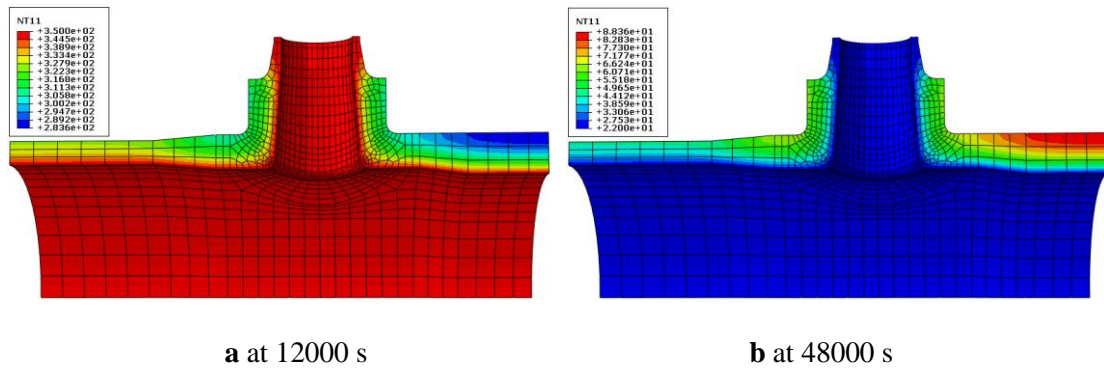
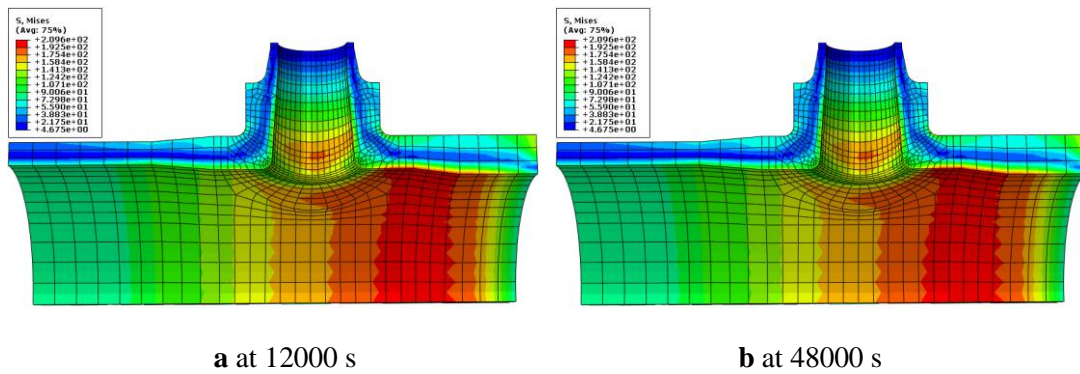
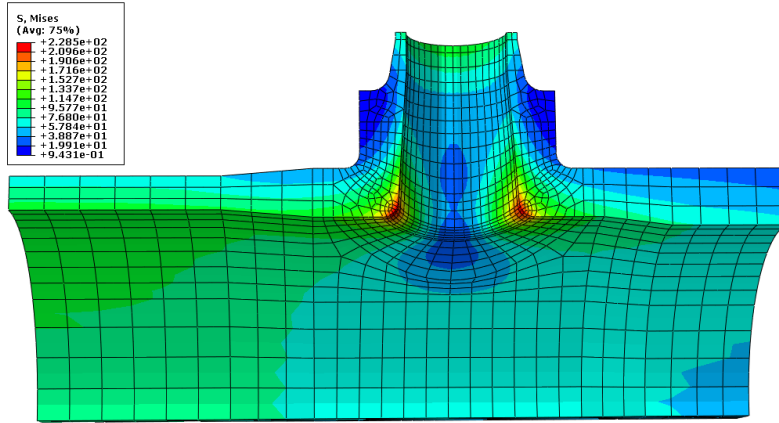


Fig. 21. Temperature distributions of the thick vessel with nozzles.



629

Fig. 22. Von Mises elastic stress field of the thick vessel with nozzles under thermal load.



630

631 **Fig. 23.** Von Mises elastic stress field of the thick vessel with nozzles under internal pressure.

632 *5.3.2 Shakedown analysis*

633 The SCM is used to calculate the shakedown limit of the thick vessel with nozzles.

634 Considering the randomness of the varying temperature gradient and internal pressure, four

635 vertices are used to define the loading domain (Fig. 24), which include two instants for

636 thermal load at $t = 12000$ and 48000 s and two instants for pressure load at $P = 0$ and 15.5

637 MPa. The applied total elastic stress history consists of thermal and pressure components:

638 σ_{θ_0} is the von Mises elastic thermal stress which is associated with the current thermal load

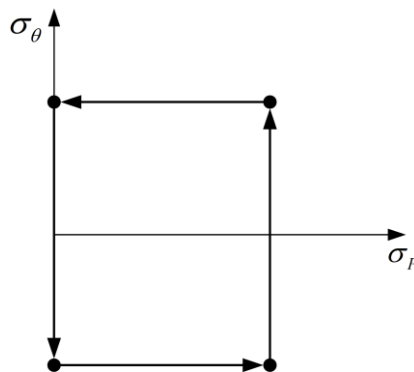
639 θ_0 , and σ_{P_0} is the von Mises elastic stress corresponding to the internal pressure

640 $P_0 = 15.5$ MPa. The load multiplier λ is determined so that $\lambda\sigma_{\theta_0}$ and $\lambda\sigma_{P_0}$ become the

641 shakedown limit, for various proportions of the two components. For the simplicity of

642 description, the angle φ ranging from 0° to 90° is introduced to denote the different

643 proportions of the two stress components.



644

645

Fig. 24. Loading domain and its vertices.

646 On basis of the previously calculated elastic stress fields (Fig. 22 and Fig. 23), the
647 shakedown limit multipliers λ are computed for different angles φ in two-dimensional
648 loading space considering the thermal load σ_θ and mechanical load σ_p varying
649 independently. The numerical results of the shakedown analysis by the SCM as well as the
650 corresponding computing time are all listed in Table 4. The shakedown domain of the thick
651 vessel with nozzles is shown in Fig. 25.

652 The shakedown boundary curve is defined by three segments with the intersection points
653 at $\varphi = 30^\circ$ and $\varphi = 56^\circ$, which are plotted in Fig. 25 additionally. It is worth noting that the
654 three segments of shakedown boundary are all dominated by alternating plasticity mechanism,
655 and the difference is due to the different locations of the maximum von Mises stress point.

656 Under various combinations of the mechanical and thermal loads, all the calculations by
657 the SCM for shakedown analyses of the thick vessel with nozzles present good convergence.
658 As an example, Fig. 26 depicts the iterative convergence process of the shakedown multiplier
659 for the load combination $\sigma_\theta/\sigma_{\theta_0} = \sigma_p/\sigma_{p_0}$ which corresponds to $\varphi = 45^\circ$. It is worth noting
660 that although the procedure initiates at a relatively high load multiplier, the load multiplier
661 decreases rapidly to a steady value, and then it approaches smoothly to the shakedown limit.
662 Moreover, the von Mises residual stress field of the thick vessel with nozzles for this case is
663 shown in Fig. 27 when the shakedown limit reaches.

664 According to the conclusions in [12], the shakedown limit of the thick vessel with nozzles
665 is the minimum one of its plastic limit and its double elastic limit when the system is
666 subjected to the single internal pressure. For the applied internal pressure $P_0 = 15.5$ MPa, the
667 maximum von Mises elastic stress occurs at the corner of the vessel with nozzles (Fig. 23)
668 and its value is 217.9 MPa. Therefore, the corresponding shakedown limit multiplier λ
669 (according to double elastic limit criterion) under the internal pressure is calculated as
670 follows:

$$671 \quad \lambda = \frac{2 \times 200 \text{MPa}}{217.9 \text{MPa}} = 1.836 \quad (44)$$

672 The value is in excellent agreement with the numerical result by the SCM, which has the
673 same load multiplier 1.836. This also indicates that the alternating plasticity mechanism is
674 decisive for the failure of the thick vessel with nozzles under the single internal pressure.

675 In order to evaluate the computational efficiency of the novel SCM for shakedown
676 analysis, the CPU time to calculate shakedown limit of the thick vessel with nozzles under
677 load combination $\sigma_P/\sigma_{P_0} = \sigma_\theta/\sigma_{\theta_0}$ by the SCM, the linear matching method (LMM) [38]
678 and the step-by-step analysis are compared in Table 5. It can be seen from Table 5 that, with
679 necessary accuracy of these calculations, the CPU time by the step-by-step analysis is more
680 than 40 times that by the SCM while the CPU time by the LMM is about 3 times that by the
681 SCM. The usage of the SCM is much cheaper and more efficient than the LMM and the
682 step-by-step analysis.

683 **Table 4** Numerical results and computing time for the shakedown analysis of the thick vessel
684 with nozzles.

φ	σ_P/σ_{P_0}	$\sigma_\theta/\sigma_{\theta_0}$	CPU time (s)
0°	1.836	0	190
5°	1.671	0.146	193
10°	1.531	0.270	211
15°	1.410	0.378	187
20°	1.301	0.474	190
25°	1.203	0.561	186
30°	1.112	0.642	209
35°	1.021	0.715	199
40°	0.934	0.784	195
45°	0.851	0.851	185
50°	0.768	0.915	187
55°	0.687	0.981	188
56°	0.669	0.992	160
60°	0.586	1.014	156
70°	0.388	1.066	151
80°	0.196	1.113	130
90°	0	1.160	128

685

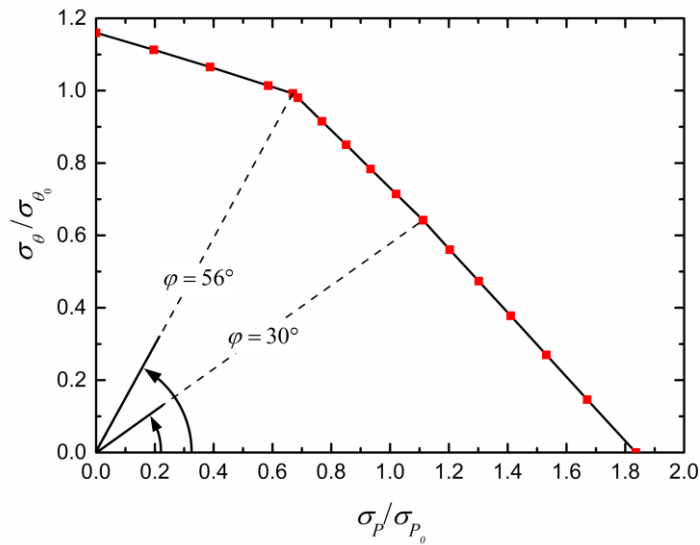
686

687

Table 5 Comparison of the CPU time by the SCM, the LMM and the step-by-step analysis.

Method	Shakedown limit multiplier	CPU time (s)
The SCM	0.851	185
The LMM	0.859	642
The step-by-step analysis	0.853	7758

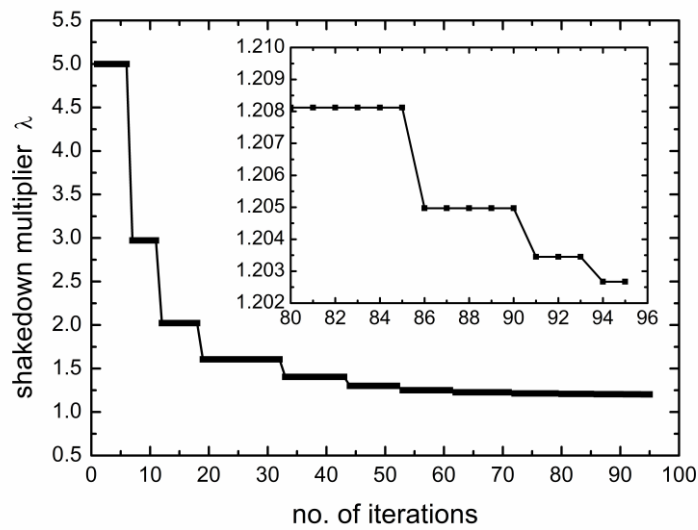
688



689

690

Fig. 25. Shakedown domain for the thick vessel with nozzles.



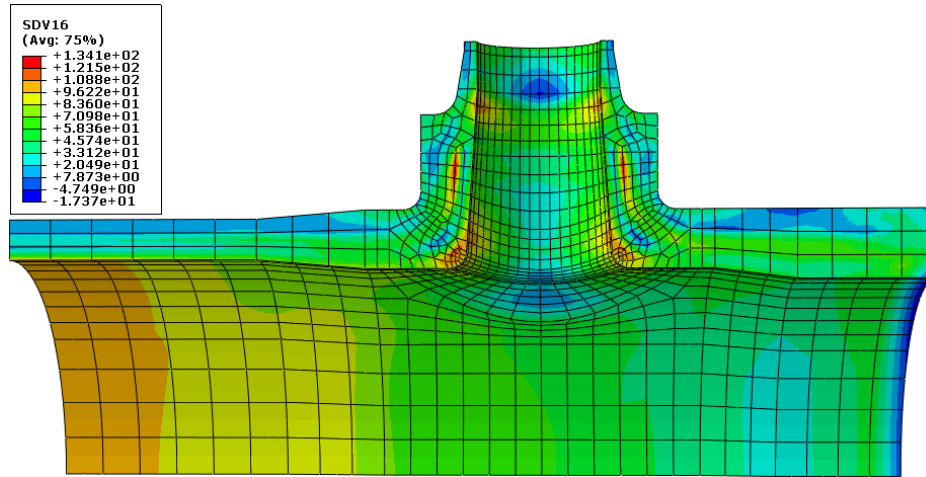
691

692

Fig. 26. Iterative convergence process of the shakedown multiplier for the load combination

693

$$\sigma_{\theta} / \sigma_{\theta_0} = \sigma_P / \sigma_{P_0} .$$



694
695 **Fig. 27.** Von Mises residual stress field of the thick vessel with nozzles for the load

696 combination $\sigma_\theta / \sigma_{\theta_0} = \sigma_P / \sigma_{P_0}$.

697 **6 Conclusions**

698 A novel numerical procedure based on the Stress Compensation Method (SCM) for
699 shakedown analysis of engineering structures under multiple variable mechanical and thermal
700 loads is proposed. The presented methodology has been implemented into ABAQUS platform
701 to investigate the Bree problem and the shakedown domains of a square plate with a central
702 circular hole under various three-dimensional loading domains, and to solve the practical
703 shakedown problems of a thick vessel with nozzles. The following conclusions can be made:

- 704 1. With no need to perform mathematical programming, the proposed numerical method for
705 shakedown analysis is a two-level iterative procedure, where just a series of linear finite
706 element analyses with same global stiffness matrix are performed and the global stiffness
707 matrix is decomposed only once. The novel strategy for constructing the residual stress
708 field makes the global equilibrium equations solved only at the end of a load cycle
709 instead of at every load vertex. Therefore, the computational cost of shakedown analysis
710 has little relationship with the number of vertices of loading domain.
- 711 2. Three types of the Bree problem verify the effectiveness of the SCM. Three shakedown
712 domains of the square plate with a circular hole under three loading cases are obtained
713 and different mechanisms involving alternating plasticity and ratcheting to determine the
714 shakedown boundaries are revealed. For the thick vessel with nozzles under the given

715 loading cases, the shakedown boundaries are dominated by the alternating plasticity
716 mechanism.

717 3. The iterative process of shakedown analysis by the SCM presents good convergence. The
718 proposed numerical procedure turns out to be of good numerical stability, high accuracy
719 and efficiency, and is well suited for shakedown analysis of large-scale engineering
720 structures under multi-dimensional loading domain.

721 4. Although the present applications are limited to the elastic-perfectly plastic material with
722 von Mises yield surface and the material properties are independent of the temperature,
723 the extensions to consideration of the hardening material and the temperature-dependent
724 yield stress are in progress, and the results will be reported in forthcoming works.

725 **Acknowledgments**

726 The authors would like to acknowledge the support of the National Science Foundation
727 for Distinguished Young Scholars of China (Grant No.11325211), the National Natural
728 Science Foundation of China (Grant No.11672147) and the Project of International
729 Cooperation and Exchange NSFC (Grant No. 11511130057) during this work.

730 **References**

- 731 [1] Borkowski A, Kleiber M. On a numerical approach to shakedown analysis of structures. *Comput*
732 *Method Appl M* 1980;22:101-119.
- 733 [2] Kleiber M, König JA. Incremental shakedown analysis in the case of thermal effects. *Int J Numer*
734 *Meth Eng* 1984;20:1567-1573.
- 735 [3] Melan E. Zur Plastizität des räumlichen Kontinuums. *Ingenieur-Archiv* 1938;9:116-126.
- 736 [4] Koiter WT, General theorems for elastic-plastic solids, in: Sneddon, JN, Hill, R (Eds.) *Progress in*
737 *Solid Mechanics*, North-Holland: Amsterdam, 1960, pp. 167-221.
- 738 [5] König JA, *Shakedown of elastic-plastic structures*, Elsevier, Amsterdam, 1987.
- 739 [6] Maier G. Shakedown theory in perfect elastoplasticity with associated and nonassociated flow
740 laws: A finite element linear programming approach. *Meccanica* 1969;4:250-260.
- 741 [7] Li HX. Kinematic shakedown analysis under a general yield condition with non-associated plastic
742 flow. *Int J Mech Sci* 2010;52:1-12.
- 743 [8] Weichert D, Hachemi A. Influence of geometrical nonlinearities on the shakedown of damaged
744 structures. *Int J Plasticity* 1998;14:891-907.
- 745 [9] Polizzotto C, Borino G, Caddemi S, Fuschi P. Theorems of restricted dynamic shakedown. *Int J*
746 *Mech Sci* 1993;35:787-801.
- 747 [10] Maier G, Novati G. *Dynamic Shakedown and Bounding Theory for a Class of Nonlinear*

- 748 Hardening Discrete Structural Models. *Int J Plasticity* 1990;6:551-572.
- 749 [11] Hachemi A, Weichert D. Application of shakedown theory to damaging inelastic material under
750 mechanical and thermal loads. *Int J Mech Sci* 1997;39:1067-1076.
- 751 [12] Stein E, Huang Y. An analytical method for shakedown problems with linear kinematic hardening
752 materials. *Int J Solids Struct* 1994;31:2433-2444.
- 753 [13] Nayebi A, El Abdi R. Shakedown analysis of beams using nonlinear kinematic hardening
754 materials coupled with continuum damage mechanics. *Int J Mech Sci* 2008;50:1247-1254.
- 755 [14] Leu SY, Li JS. Shakedown analysis of truss structures with nonlinear kinematic hardening. *Int J*
756 *Mech Sci* 2015;103:172-180.
- 757 [15] Le CV, Tran TD, Pham DC. Rotating plasticity and nonshakedown collapse modes for elastic-
758 plastic bodies under cyclic loads. *Int J Mech Sci* 2016;111-112:55-64.
- 759 [16] Simon JW. Direct evaluation of the limit states of engineering structures exhibiting limited,
760 nonlinear kinematical hardening. *Int J Plasticity* 2013;42:141-167.
- 761 [17] Belytschko T. Plane stress shakedown analysis by finite elements. *Int J Mech Sci*
762 1972;14:619-625.
- 763 [18] Janas M, Pycko S, Zwoliński J. A min-max procedure for the shakedown analysis of skeletal
764 structures. *Int J Mech Sci* 1995;37:629-643.
- 765 [19] Xue MD, Wang XF, Williams FW, Xu BY. Lower-bound shakedown analysis of axisymmetric
766 structures subjected to variable mechanical and thermal loads. *Int J Mech Sci* 1997;39:965-976.
- 767 [20] Zouain N, Borges L, Silveira JL. An algorithm for shakedown analysis with nonlinear yield
768 functions. *Comput Method Appl M* 2002;191:2463-2481.
- 769 [21] Khoi VUD, Yan A-M, Hung N-D. A dual form for discretized kinematic formulation in
770 shakedown analysis. *Int J Solids Struct* 2004;41:267-277.
- 771 [22] Vu DK, Yan AM, Nguyen-Dang H. A primal-dual algorithm for shakedown analysis of structures.
772 *Comput Method Appl M* 2004;193:4663-4674.
- 773 [23] Makrodimopoulos A, Martin CM. Lower bound limit analysis of cohesive-frictional materials
774 using second-order cone programming. *Int J Numer Meth Eng* 2006;66:604-634.
- 775 [24] Bisbos CD, Makrodimopoulos A, Pardalos PM. Second-order cone programming approaches to
776 static shakedown analysis in steel plasticity. *Optim Method Softw* 2005;20:25-52.
- 777 [25] Krabbenhoft K, Lyamin AV, Sloan SW. Shakedown of a cohesive-frictional half-space subjected
778 to rolling and sliding contact. *Int J Solids Struct* 2007;44:3998-4008.
- 779 [26] Nguyen AD, Hachemi A, Weichert D. Application of the interior-point method to shakedown
780 analysis of pavements. *Int J Numer Meth Eng* 2008;75:414-439.
- 781 [27] Garcea G, Leonetti L. A unified mathematical programming formulation of strain driven and
782 interior point algorithms for shakedown and limit analysis. *Int J Numer Meth Eng*
783 2011;88:1085-1111.
- 784 [28] Simon JW, Weichert D. Numerical lower bound shakedown analysis of engineering structures.
785 *Comput Method Appl M* 2011;200:2828-2839.
- 786 [29] Simon JW, Weichert D. Shakedown analysis with multidimensional loading spaces. *Comput*
787 *Mech* 2012;49:477-485.
- 788 [30] Liu YH, Zhang XF, Cen ZZ. Lower bound shakedown analysis by the symmetric Galerkin
789 boundary element method. *Int J Plasticity* 2005;21:21-42.
- 790 [31] Le CV, Nguyen-Xuan H, Askes H, Bordas SPA, Rabczuk T, Nguyen-Vinh H. A cell-based
791 smoothed finite element method for kinematic limit analysis. *Int J Numer Meth Eng*

792 2010;83:1651-1674.

793 [32] Tran TN, Liu GR, Nguyen-Xuan H, Nguyen-Thoi T. An edge-based smoothed finite element
794 method for primal–dual shakedown analysis of structures. *Int J Numer Meth Eng*
795 2010;82:917-938.

796 [33] Nguyen-Xuan H, Rabczuk T, Nguyen-Thoi T, Tran TN, Nguyen-Thanh N. Computation of limit
797 and shakedown loads using a node-based smoothed finite element method. *Int J Numer Meth Eng*
798 2012;90:287-310.

799 [34] Chen S, Liu Y, Cen Z. Lower bound shakedown analysis by using the element free Galerkin
800 method and non-linear programming. *Comput Method Appl M* 2008;197:3911-3921.

801 [35] Do HV, Nguyen-Xuan H. Limit and shakedown isogeometric analysis of structures based on
802 Bézier extraction. *European Journal of Mechanics - A/Solids* 2017;63:149-164.

803 [36] Ponter ARS, Carter KF. Shakedown state simulation techniques based on linear elastic solutions.
804 *Comput Method Appl M* 1997;140:259-279.

805 [37] Ponter ARS, Engelhardt M. Shakedown limits for a general yield condition: implementation and
806 application for a Von Mises yield condition. *Eur J Mech a-Solid* 2000;19:423-445.

807 [38] Chen HF, Ponter ARS. Shakedown and limit analyses for 3-D structures using the linear matching
808 method. *International Journal of Pressure Vessels and Piping* 2001;78:443-451.

809 [39] Chen HF, Ponter ARS. A method for the evaluation of a ratchet limit and the amplitude of plastic
810 strain for bodies subjected to cyclic loading. *Eur J Mech a-Solid* 2001;20:555-571.

811 [40] Lytwyn M, Chen HF, Ponter ARS. A generalised method for ratchet analysis of structures
812 undergoing arbitrary thermo-mechanical load histories. *Int J Numer Meth Eng* 2015;104:104-124.

813 [41] Spiliopoulos KV, Panagiotou KD. A Residual Stress Decomposition based Method for the
814 Shakedown analysis of structures. *Comput Method Appl M* 2014;276:410-430.

815 [42] Tin-Loi F, Ngo NS. Performance of a p-adaptive finite element method for shakedown analysis.
816 *Int J Mech Sci* 2007;49:1166-1178.

817 [43] Groß-Weege J. On the numerical assessment of the safety factor of elastic-plastic structures under
818 variable loading. *Int J Mech Sci* 1997;39:417-433.

819 [44] Chinh PD. Evaluation of shakedown loads for plates. *Int J Mech Sci* 1997;39:1415-1422.

820 [45] Barbera D, Chen H, Liu Y, Xuan F. Recent Developments of the Linear Matching Method
821 Framework for Structural Integrity Assessment. *Journal of Pressure Vessel Technology*
822 2017;139:051101-051109.

823 [46] Spiliopoulos KV, Panagiotou KD. A numerical procedure for the shakedown analysis of structures
824 under cyclic thermomechanical loading. *Arch Appl Mech* 2015;85:1499-1511.

825 [47] ABAQUS. Dassault Systems, Version 6.14, 2014.

826 [48] Bree J. Elastic-plastic behaviour of thin tubes subjected to internal pressure and intermittent
827 high-heat fluxes with application to fast-nuclear-reactor fuel elements. *Journal of strain analysis*
828 1967;2:226-238.

829 [49] Bradford RAW. The Bree problem with primary load cycling in-phase with the secondary load.
830 *International Journal of Pressure Vessels and Piping* 2012;99–100:44-50.

831 [50] Garcea G, Armentano G, Petrolo S, Casciaro R. Finite element shakedown analysis of
832 two-dimensional structures. *Int J Numer Meth Eng* 2005;63:1174-1202.

833